

FLORIDA STATE UNIVERSITY
COLLEGE OF ARTS AND SCIENCE

MAGNETIC SHIELDING OF PHOTOTUBES USED WITH NAI(TL) DETECTORS FROM EXTERNAL
MAGNETIC FIELDS

By

CHRISTOPHER E. MERTIN

Thesis submitted to the Department of Physics
in partial fulfillment of the requirements for
the degree of Bachelors of Science

Degree Awarded:
Spring Semester, 2015

Christopher E. Mertin defended this thesis on April 22, 2014.

The members of the Defense Committee approve the thesis defended on this date.

Ingo Wiedenhöver
Professor Directing Thesis

Todd Adams
Committee Member

Philip Bowers
University Representative

ACKNOWLEDGMENTS

I would like to express my gratitude to Dr. Ingo Wiedenhöver for giving me the opportunity to do research under him all these years and being a great mentor, especially for this thesis. The other members of my committee, Dr. Todd Adams and Dr. Philip Bowers, deserve hazard pay for not only having to put up with me, but also for the length of this paper and I'm grateful that they served on my defense committee. Special thanks is also deserved for Dr. Daniel Santiago for helping me get started with this project and helping me debug code a few times when I hit a brick wall, Sean Kuvin and Dr. Lagy Baby for helping me with various tasks dealing with the NaI(Tl) detectors and the solenoid used in this research project, and my good friend Medalla who kept me strong throughout this writing process.

ABSTRACT

The John D. Fox Superconducting Accelerator at Florida State University houses experiments for nuclear physics research. One of these experiments deals with a gamma ray detector array that is located close to a superconducting solenoid. This work looks at the possibility of being able to upgrade this detector array with newer equipment, resulting in a higher resolution. However, this upgrade makes these detectors much more sensitive to magnetic fields produced by the solenoid, thus techniques were investigated to mitigate these problems. This was done by analyzing, via simulations, the use of an active shield to partially cancel the magnetic field, and a passive shield to redirect the residual magnetic field in a given area. The results from this work show that reducing the magnetic field down to operational levels is possible and allows this upgrade to be implemented.

TABLE OF CONTENTS

Abstract	iv
1 Introduction	1
1.1 NaI(Tl) Detectors – Scintillation Crystal	1
1.2 NaI(Tl) Detectors – Photomultiplier Tubes	3
1.3 NaI(Tl) Detector Array & the Solenoid	10
2 Magnetic Fields & Magnetic Shields	13
2.1 Magnetic Field from a Solenoid	13
2.2 Magnetic Shielding	14
2.2.1 Passive Shielding	14
2.2.2 MuMetal as a Passive Shield	17
2.2.3 Effects of Mechanical Stress on MuMetal	19
2.2.4 Active Shielding	21
2.3 Simulating the Magnetic Field	22
2.3.1 Numerical Integration Technique	26
3 Results	28
3.1 Magnetic Field from the Solenoid	28
3.1.1 Active Shielding with a Helmholtz Coil	29
3.1.2 Passive Shielding with MuMetal	31
3.2 Conclusion	37
Appendices	
A Derivations	38
A.1 Off-Axis Biot-Savart Equations	38
A.2 Magnetic Field in a Helmholtz Coil	40
B Source Code	43

CHAPTER 1

INTRODUCTION

The John D. Fox Superconducting Accelerator at Florida State University houses equipment for various nuclear physics experiments. One of the experiments uses RESOLUT, a system used for the study of beams of short-lived nuclei. Recently, a NaI(Tl) detector array was installed to be used alongside RESOLUT, placing this array in the presence of a magnetic field from a superconducting solenoid, where this magnetic field then causes problems with the Photomultiplier Tubes (PMT's) used in measurements. Therefore, the point of this project was to reduce the magnetic field the PMT's experience so that they can perform at their optimum efficiency, with the ultimate end result of being able to use a new set of PMT's which have a higher resolution, though much more sensitive to magnetic fields when compared to the ones currently in use.

1.1 NaI(Tl) Detectors – Scintillation Crystal

Scintillators are used in detecting all types of radiation and come in two major categories. Organic scintillators are commonly used in the detection of beta-decay reactions and neutrons, while inorganic scintillators are mainly used in detecting gamma rays.

The detectors used in this project are composed of a sodium iodide crystal containing trace amounts of thallium, on the order of 10^{-3} mole fractions¹. The benefit of sodium iodide is the large proton number of iodine ($Z=53$) which allows for easy ionization of orbiting electrons. The thallium is called an activator in the crystal and helps in quickly creating detectable photons from the incident gamma ray. Figure 1.1 shows how this scintillation process occurs.

The detection method in the crystal is based on the discrete electron excitation energies that are determined by the crystal lattice of sodium iodide. These two energy bands are classified as the valence band and the conduction band. The valence band contains electrons which are bound to the lattice structure, while the conduction band is composed of electrons which have sufficient energy to move around the crystal. The area between these two bands is known as the band gap where no excited states are found in a pure sodium iodide lattice.

¹Mole fractions in this instance is the number of moles of NaI to Tl in the crystal. 10^{-3} mole fractions of thallium corresponds to 1 mole of thallium for every 1000 moles of sodium iodide.

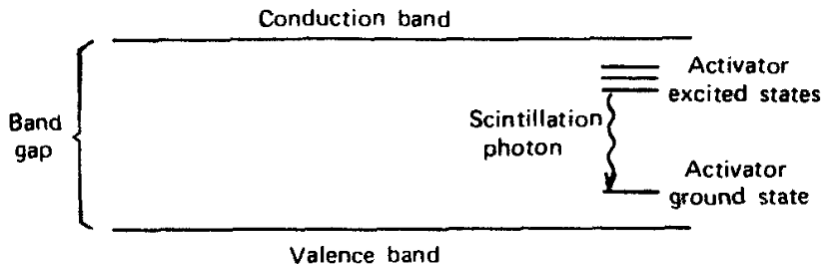


Figure 1.1: Conduction and valence band in an inorganic scintillator. The activator states come about from the small amounts of activator which are located in the crystal and create excited states within the band gap [1].

The incident gamma ray deposits its energy in the crystal, causing electrons to become excited and creating electron-hole pairs by promoting electrons from the valence band to the conduction band. In a pure sodium iodide crystal, these rogue electrons de-excite back to the valence band and release a photon that is approximately equal to the energy used to excite it into the conduction band. This emitted photon then travels through the crystal until it comes into contact with another sodium iodide atom, at which point another electron becomes excited and repeats this process. This is a slow and inefficient process and any emitted photons will be difficult to detect as their energy lies outside of the visible spectrum.

This is where the addition of small amounts of thallium start to become important. These thallium atoms are present in parts of the sodium iodide lattice structure and are known as the activator sites in Figure 1.1. These activator sites modify the energy bands located in a pure sodium iodide lattice by creating excited states that are within the band gap. In this instance, after the creation of an electron-hole pair, the positive-hole is attracted towards the activator site and ionizes the thallium atom as the energy of the hole is generally greater than the energy of the bound electron. The electrons that are promoted into the conduction band from the incident gamma ray migrate around the crystal until finding a positive-hole at an activator site, at which point it will de-excite into an excited thallium atom state and then further drop to the thallium's ground state. In transitioning to the ground state, a photon is emitted that is less energy than the NaI band gap, for which the NaI crystal is transparent. This is due to the fact that the energy of this photon is not enough to excite any of the electrons in a sodium iodide atom, and the abundance of thallium in the crystal is too small for many interactions to occur.

The number of electrons that undergo this process is directly proportional to the energy of the incident gamma ray. Therefore, the higher the energy of the incident gamma ray the more electrons that are promoted into the band gap and the more photons are emitted towards the PMT's to be detected.

1.2 NaI(Tl) Detectors – Photomultiplier Tubes

The PMT's detect the photons that are emitted in the scintillation process. In order to completely understand why the PMT's lose sensitivity in magnetic fields, how the PMT's function needs to be fully understood, where a diagram of a PMT's functioning components is depicted in Figure 1.2. As the incident photon hits the photocathode (object 15 in Figure 1.2), an electron is emitted with an energy equal to

$$E_{e^-} = h\nu - \phi_p \quad (1.1)$$

where h is Planck's constant, ν is the frequency of the photon, and ϕ_p is the workfunction of the photocathode. This workfunction is an inherent potential barrier that the electron must overcome to be emitted into the PMT. The energy of emitted photoelectrons is on the order of 1 eV or less, so their energy must be increased as in this energy range they would be impossible to detect. This is done by accelerating the electrons via an electric field which can be created by a potential difference at the electron's location. The relation between the electric field created by such a potential difference can be represented by

$$\mathbf{E} = -\nabla V \quad (1.2)$$

where V is a scalar representing the potential difference at the electron's location and \mathbf{E} is the electric field. The geometrical interpretation of this equation is the electric field points in the direction of maximum increase of the potential, V . To create this electric field, a potential is applied to the first dynode (object 1 in Figure 1.2), and the focusing electrodes (object 14 in Figure 1.2), with a larger potential being applied to the first dynode. This causes the electrons to be accelerated toward the first dynode, while the focusing electrodes reduce the cross-section of the electrons to insure they strike the first dynode. The overall force that the electron feels from this electric field is represented as

$$\mathbf{F} = q\mathbf{E} \quad (1.3)$$

where q is the charge of the particle and \mathbf{E} is the electric field that is created by the potential difference. This force causes the electrons to accelerate towards the first dynode, with the amount of energy of the

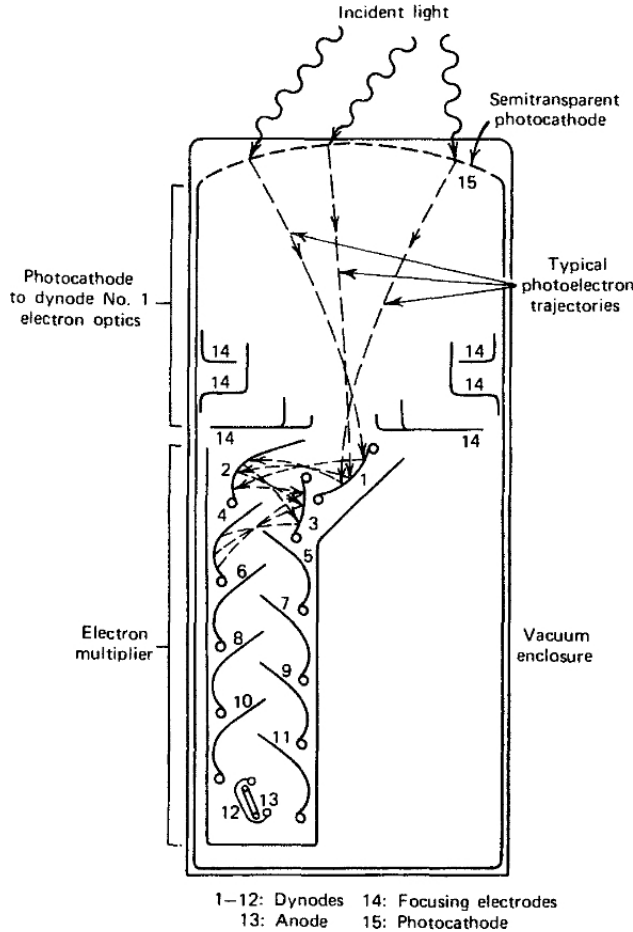


Figure 1.2: Individual components of a Photomultiplier Tube. Dashed lines indicate path of electrons [2].

electron at arrival due to the electric field can be found by integrating Equation (1.3) over the electron's path. Therefore, the total energy of the electron at arrival would be

$$\mathcal{U} = -q \int_0^D \mathbf{E} \cdot d\ell + E_{e^-} \quad (1.4)$$

where D is the distance from the photocathode to the dynode which was arbitrarily placed at zero, and the negative sign being introduced to switch the integration bounds. The initial energy of the photoelectron can be neglected as the energy obtained by the electric field is the dominating term, resulting in the kinetic energy of the electron as it strikes the dynode being completely determined by the acceleration it undergoes from the electric field.

Upon striking the dynode, the energetic electron deposits its energy in the material which excites electrons at the dynode's surface. In order for electrons to be ejected from the dynode, they must obtain the ionization energy of the material for them to be ejected. The number of electrons that are ejected from the surface is proportional to the kinetic energy of the incident electron, meaning larger potentials result in more electrons being emitted. These electrons are then ejected from the first dynode with small amounts of kinetic energy, on the order of a few eV, and experience an electric field from the second dynode (object 2 in Figure 1.2).

This electric field is due to a potential being applied to the second dynode that is greater than the first, causing any secondary electrons to accelerate towards the second dynode, where the above steps are repeated resulting in more electrons being ejected from the surface of the second dynode. This trend continues throughout the dynode chain as each successive dynode (objects 3–12 in Figure 1.2) has a higher potential than the last, multiplying the electrons in each step. These are then collected at the anode (object 13 in Figure 1.2), which measures the current as the electrons pass through. The current that passes through the anode is therefore proportional to the energy of the original gamma ray that struck the NaI(Tl) crystal, as a larger current would correspond to more photons striking the photomultiplier tube.

As the electrons travel down the PMT, outside forces can influence their path and cause changes in their energy. In the case of this project, the superconducting magnet creates a static magnetic field at the PMT's location, which brings about an additional term in the force that the electrons experience. This contribution from the magnetic field transforms Equation (1.3) into what is known as the Lorentz Force law, which is defined as

$$\mathbf{F} = q(\mathbf{E} + \mathbf{v} \times \mathbf{B}) \quad (1.5)$$

where \mathbf{F} is the force that the charged particle feels, \mathbf{v} is the velocity of the particle, q is its charge, and \mathbf{E} and \mathbf{B} are the electric and magnetic fields, respectively, that the charged particle is traveling through. In Equation (1.5), the magnetic force is always perpendicular to the velocity, resulting in magnetic fields only being able to vary a charged particle's path and not its kinetic energy. This is how magnetic fields cause problems with PMT's, by altering the paths of electrons such that they don't reach the anode at the end.

However, not all photomultiplier tubes behave the same in the presence of a magnetic field which is due to the structural differences in their dynodes. The PMT's currently being used in the NaI(Tl) array are Hamamatsu H2611, which are composed of various layers of fine-mesh dynodes. These fine-mesh PMT's

were originally designed for the purpose of being used in the presence of high magnetic fields. Figure 1.3 shows a detailed depiction of this type of PMT and how it operates.

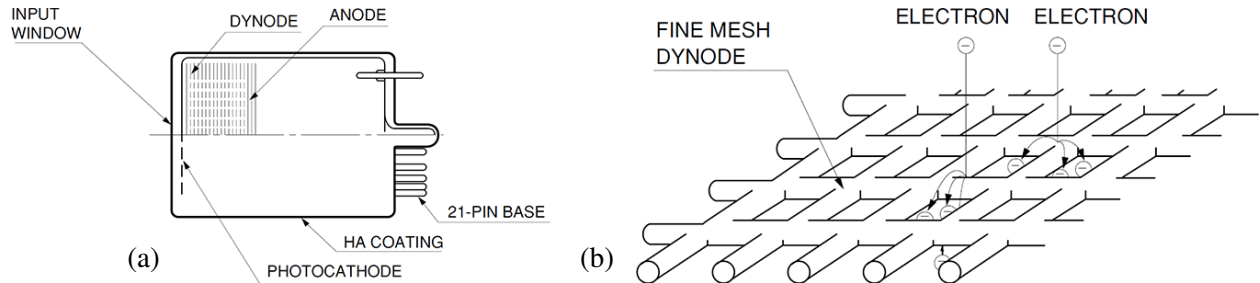


Figure 1.3: Shape of the fine-mesh PMT that is currently installed on the detector array. Figure (a) shows the overall picture of the PMT, where the incident photon strikes the photocathode on the left, causing the ejected photoelectron to travel through to the fine-mesh of dynodes on the right. Figure (b) shows how the fine-mesh dynodes behave as an electron strikes them. As the electrons come into contact with the dynode's surface, the dynode emits secondary electrons which "fall" through the holes in the mesh to the next dynode layer. The number of electrons ejected from the dynode's surface is proportional to the energy of the initial electron, and this trend continues throughout the length of the PMT until they are collected at the anode [3].

The electrons are attracted towards the fine-mesh dynodes due to a potential being applied to them, and upon striking the dynode surface, secondary electrons are emitted and "fall" through the holes in the dynode mesh. These secondary electrons will then repeat this process with each successive dynode until reaching the anode at the end. These types of PMT's are not as susceptible to magnetic fields for a few reasons. The major reason is that the electrons, including the initial photoelectron, do not travel large distances before coming into contact with a dynode. The other leading factor is that there are many sections of the dynode mesh which the electron can strike, thus any changes in its trajectory are much less likely to cause the electron to miss striking any dynode surface.

PMT's with this type of dynode structure do not have very high resolution since the electrons are less controlled and have the ability to move around more. This is not an ideal case as using higher resolution PMT's in the NaI(Tl) array are preferred for more accurate measurements. The alternative PMT that is to be used is the Hamamatsu R2154, which has a different dynode structure, leading to a greater timing resolution. This also has consequences in its behavior in magnetic fields and makes them much more sensitive. Figure 1.4 shows the structure of this type of PMT and how the electrons travel to the anode.

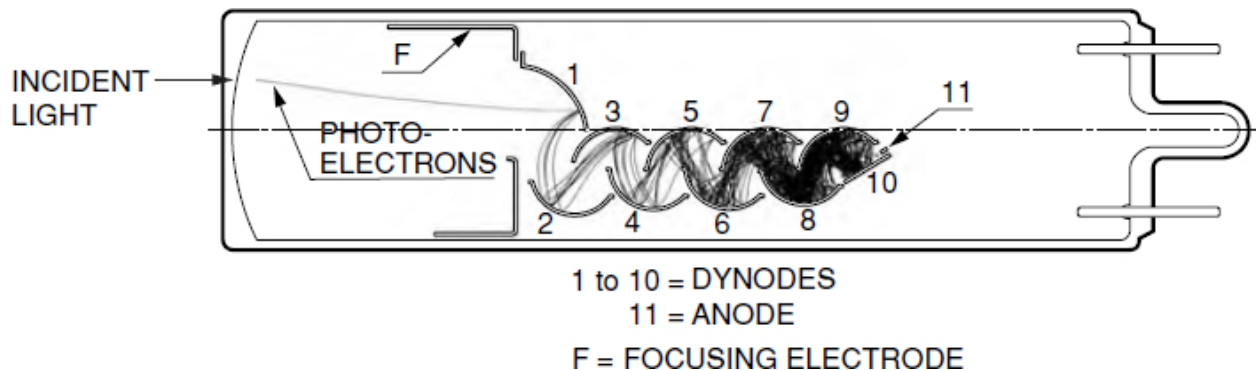


Figure 1.4: Layout of a linear dynode structure used in the R2154 PMT. Curved section on the left is the photocathode which emits the initial electrons. Lines are the results of simulated electron trajectories [3].

Individual characteristics that lead to this better timing resolution are the dominant contributors to the magnetic field sensitivity. For example, the initial photoelectrons must travel over a much larger distance to reach the first dynode when compared to the fine-mesh array. This longer distance provides magnetic fields the opportunity to apply a magnetic force on traveling electrons, causing larger variations in their paths.

The other major contributing factor is that the electrons are confined to only moving in a straight path down the PMT. As Equation (1.5) shows, the magnetic field applies the largest force when perpendicular to the path of the charged particles. This makes the R2154 PMT's more sensitive to a magnetic field with a radial component since the electrons travel in a linear fashion down the length of the PMT. Therefore, to use this type of PMT in the NaI(Tl) array, the main focus is to minimize the radial component of the external magnetic field.

Hamamatsu also provides measurements on how these PMT's behave in magnetic fields, demonstrating how the sensitivity of the PMT's varies as a function of the external field. Figure 1.5 shows how PMT's similar to the fine-mesh H2611 PMT behave in two different magnetic fields. This figure agrees with the previous conclusion that these types of photomultiplier tubes behave well in the presence of magnetic fields with low sensitivity loss, even for fields with a large radial component.

For the case of the R2154 linear type, Figure 1.6 shows the effects of a magnetic field only along its most sensitive axis, as depicted in the image to the right of the plot. The plot shows two curves for the relative outputs which are defined as with and without shielding. This shielding curve is how these PMT's behave with a Hamamatsu E989 series magnetic shield, which is not the shielding being used so it can be ignored.

In the case without a shield, the relative output varies greatly as a function of the applied magnetic field. The reason for this is due to the Lorentz Force, Equation (1.5). As stated by the Lorentz Force law, the component of the charged particle's path that is perpendicular to the magnetic field will experience a force, while any component parallel to the magnet field will not experience one. This perpendicular component will start to undergo cyclotron motion, while the parallel component will behave as if there is no magnetic field present. This mixing between the forces that the components are experiencing causes the electrons to move in a helical fashion where they will stray away from the dynodes and never be picked up by the anode, thus reducing the sensitivity of the PMT. This is where the gain-shift comes about since the number of electrons that the PMT detects is proportional to the energy of the incident gamma ray. Therefore, with the loss of electrons being detected, the PMT will register a lower energy in the signal.

In this figure, 1 A/m is the equivalent of a 0.01257 Gauss field. As seen in Figure 1.6, even with a radial field as low as 2 A/m , 0.025 G, the relative output is approximately 6% . Therefore, for the R2154 PMT's to be utilized, any radial component of the magnetic field must be lowered to a level that is less than 0.5 A/m , 0.00628 G, so minimal sensitivity loss will occur.

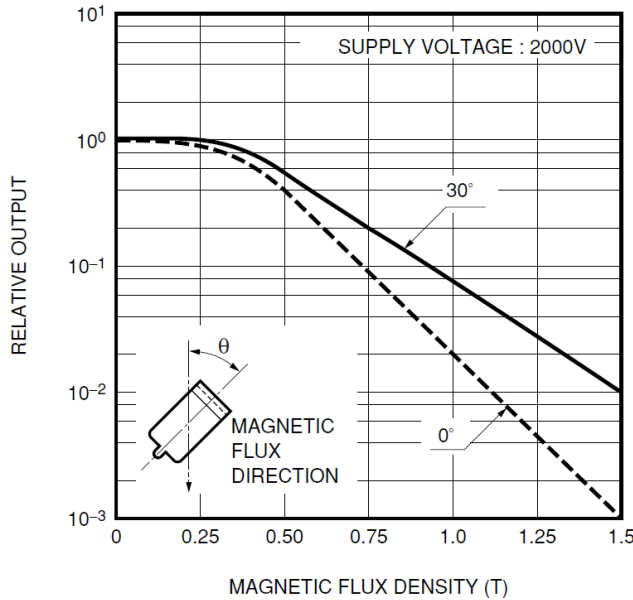


Figure 1.5: Influence of the sensitivity of fine-mesh PMT's like the Hamamatsu H2611. This plot shows that fine-mesh PMT's have the ability to be used in large magnetic fields, with magnetic fields having large radial components not being detrimental to the output, with a 90% output remaining in the presence of a 0.25 T magnetic field [3].

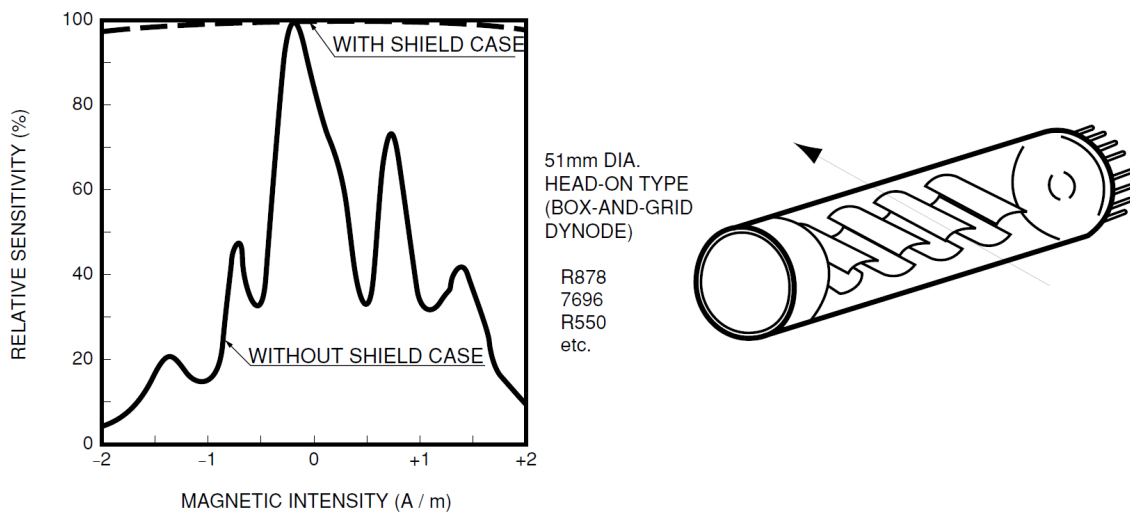


Figure 1.6: Influence of the sensitivity of PMT's like the R2154. The plot contains only measurements over the most sensitive direction, which is depicted in the diagram on the right. The shielding referred to in this plot refers to Hamamatsu E989 series magnetic shielding cases, showing how magnetic shielding helps retain the relative sensitivity of the PMT. This is not the shielding used, so the plot dealing with the shielding can be ignored. For the x -axis in the plot, 1 A/m is approximately 0.01257 Oersted, where 1 Oersted is equivalent to 1 Gauss in air [3].

1.3 NaI(Tl) Detector Array & the Solenoid

The superconducting solenoid that is creating the magnetic field causing this effect on these PMT's is housed in a cryostat. Less than 1 meter away from the end of the cryostat is the location of the PMT's being used in the NaI(Tl) array. Figure 1.7 shows a picture of the setup, with the cryostat being located on the left and the NaI detector bound with the PMT's on the right.

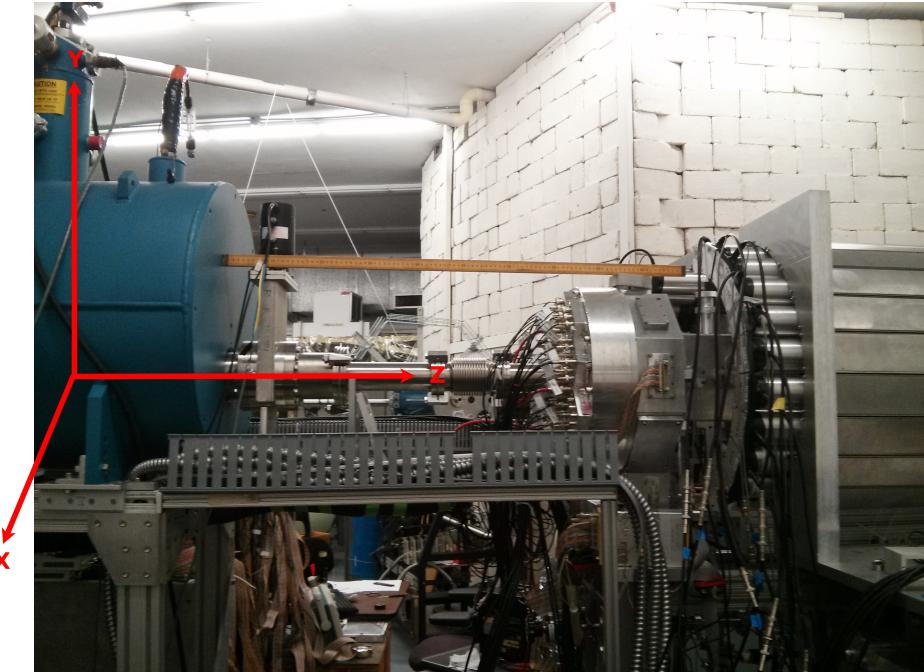


Figure 1.7: Setup of the detector array alongside the cryostat. The solenoid is located in the blue cryostat on the left and the NaI(Tl) array is on the right. Overlaid coordinate axes denote the coordinate system used for all measurements and calculations, with $(0, 0, 0)$ defined as the center of the solenoid. Meterstick placed for scale.

In this figure, red axes are overlaid to denote the coordinate system that is used for all of the calculations and measurements for this project, unless otherwise stated. In this system, the point $(0, 0, 0)$ is defined as the center of the solenoid where the components of the magnetic field are defined as the z -component traveling along the z -axis (B_z), and the radial component being defined as $\sqrt{B_x^2 + B_y^2}$. The detector array is cylindrically shaped, parallel to the z -axis, with a radius of 0.20 m, placing the PMT's at a 12.65° angle from the center of the solenoid. At locations off axis from the solenoid is where the radial component of the magnetic field comes into play.

Before being able to understand how to mitigate this shifting effect, it is important to test its severity on how it effects the H2611 PMT's. To do this, a ^{137}Cs source was tested under different magnetic field conditions, and the resulting spectra was used to determine how much of a shift occurred in these different situations. ^{137}Cs is a single gamma ray emission source, emitting a single gamma ray at 661.7 keV. This will cause a single gamma ray peak to be detected for each individual situation, allowing for the movement of this peak to be easily tracked, thus demonstrating this gain-shifting effect. The results from these measurements can be seen in Figure 1.8.

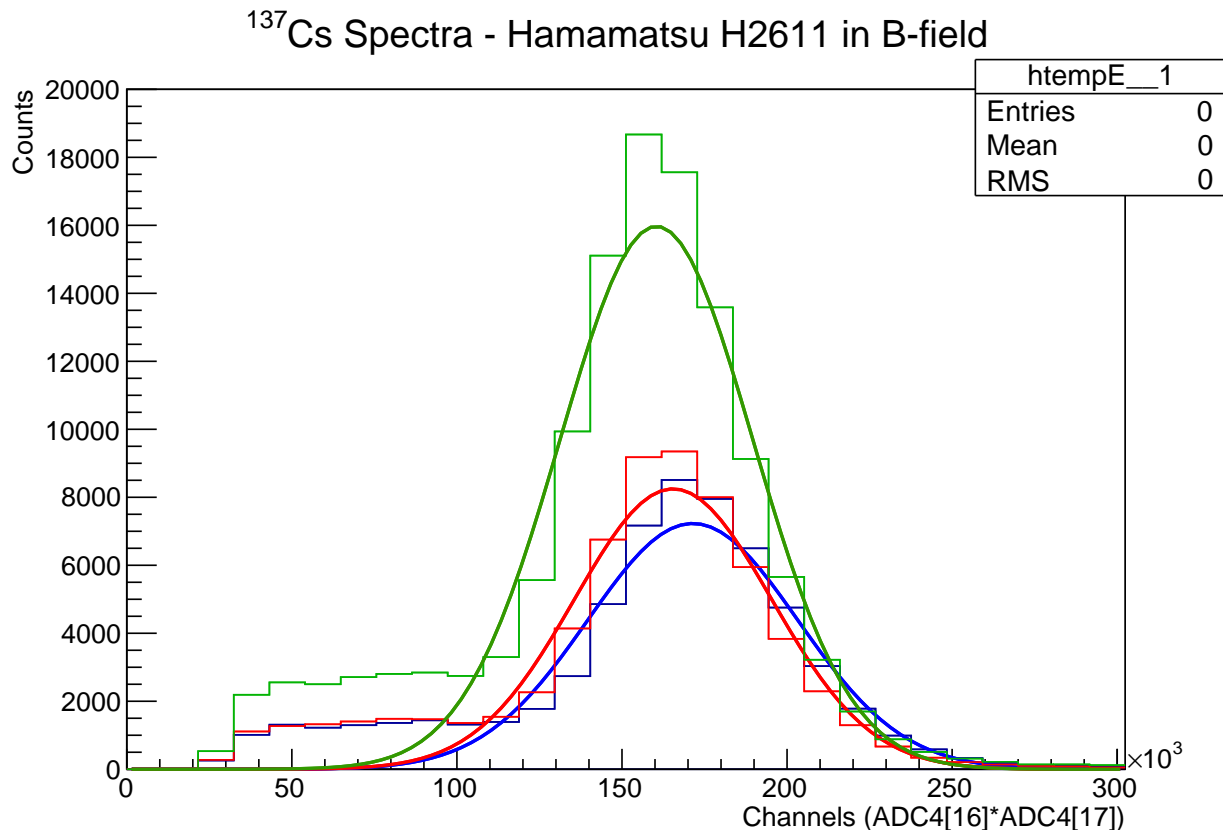


Figure 1.8: Gain Shift with current PMT's. Spectra for ^{137}Cs with the Solenoid running a current of 0 A (blue), 50 A (red), and 70 A (green). Normalization of the curves is arbitrary as each run was over different time intervals. However, the shift in the signals can still be seen.

For each individual spectra, a Gaussian fit was separately applied to the individual ^{137}Cs peaks for each run. The blue peak corresponds to the solenoid being off, the red denotes a 50 Amp current passing through the solenoid which creates a magnetic field of 32 Gauss z -component and 8 Gauss radial component magnetic

field at the PMT's location, and the green denotes a 70 Amp current through the solenoid creating a 44 Gauss z -component and a 15 Gauss radial component. As this figure shows, there is a small but significant difference between the presence and absence of a magnetic field, with minimal, however still noticeable, difference between the two cases when the solenoid was on. The newer R2154 PMT's were not tested, though as shown in the previous section, the gain-shift at these levels would be much more dramatic and would more than likely produce no signal.

CHAPTER 2

MAGNETIC FIELDS & MAGNETIC SHIELDS

2.1 Magnetic Field from a Solenoid

To be able to stop the gain shifting from the magnetic field, the radial component of the magnetic field must be known at the locations of the PMT's. However, direct measurements with a Gauss meter cannot be made at every location since the orientation of the probe needs to be exactly perpendicular to the magnetic field to obtain a precise measurement. The solution to this was to write a simulation of the solenoid which calculates the exact radial component of the magnetic field at these locations.

A difficulty with this simulation is there is no analytical solution for calculating the off-axis values of the magnetic field from a solenoid. Therefore, the solenoid was approximated as individual coil-loops, and the Biot-Savart law was used to calculate the contribution of the magnetic field from each individual coil. The Biot-Savart law for a single coil is defined as

$$\mathbf{B} = \frac{\mu_0 I}{4\pi} \int_C \frac{d\ell \times \hat{\mathbf{r}}}{|\mathbf{r}|^2} = \frac{\mu_0 I}{4\pi} \int_C \frac{d\ell \times \mathbf{r}}{|\mathbf{r}|^3} \quad (2.1)$$

where μ_0 is the permeability of free space with a value of $4\pi \times 10^{-7}$ m·kg/s²·A², I is the current traveling through the coil in units of Amperes, C is the contour over which the current flows, \mathbf{r} is the displacement vector which is defined from the location of the coil to the point being calculated ($\mathbf{r} - \mathbf{r}_c$), and $d\ell$ is the differential wire element containing the current. One constraint for the simulation in using the Biot-Savart law is that the location and radius of each coil needs to depend on the location of the prevailing coil and the dimensions of the wire. The individual x, y, z components of Equation (2.1) need to be derived as well so that the radial component of the magnetic field can be calculated. The following is the result of breaking this equation into its individual parts, where the derivation of these equations can be found in Appendix B.

$$B_x = R_0 \frac{\mu_0 I (\gamma - z_c)}{4\pi} \int_0^{2\pi} \frac{\cos(\theta)}{\left[|\alpha - R_0 \cos(\theta)|^2 + |\beta - R_0 \sin(\theta)|^2 + |\gamma - z_c|^2\right]^{3/2}} d\theta \quad (2.2)$$

$$B_y = R_0 \frac{\mu_0 I (\gamma - z_c)}{4\pi} \int_0^{2\pi} \frac{\sin(\theta)}{\left[|\alpha - R_0 \cos(\theta)|^2 + |\beta - R_0 \sin(\theta)|^2 + |\gamma - z_c|^2\right]^{3/2}} d\theta \quad (2.3)$$

$$B_z = R_0 \frac{\mu_0 I}{4\pi} \int_0^{2\pi} \frac{R_0 - \beta \sin(\theta) - \alpha \cos(\theta)}{\left[|\alpha - R_0 \cos(\theta)|^2 + |\beta - R_0 \sin(\theta)|^2 + |\gamma - z_c|^2\right]^{3/2}} d\theta \quad (2.4)$$

where (α, β, γ) are the spacial (x, y, z) coordinates where the magnetic field is to be calculated, z_c is the location along the z -axis for the coil being calculated, varying with each coil, R_0 is the radius of the coil in question, and θ is the angle relative to the differential element of the wire. With no analytical solution to these equations, numerical integration techniques had to be implemented, which are discussed in more detail in Section 2.3.1.

2.2 Magnetic Shielding

There are two types of magnetic shielding that can be used to lower the magnetic field in a given area, passive magnetic shielding, and active magnetic shielding. Both techniques are proposed here to achieve the desired results, with each individual technique being discussed in more detail below.

2.2.1 Passive Shielding

The effectiveness of a material being used as a passive shield is based on two parameters, the saturation field of the material and its permeability. A material's saturation is the limit of the magnetic flux that is able to permeate through the material for a given external magnetic field. Beyond this saturation limit, the applied magnetic field behaves as if this passive shield was non-existent. This saturation is governed by a single equation which is similar to how Ohm's law ($V = IR$) deals with circuits. This equation is known as Hopkinson's law, and deals with magnetic fields and their flux for different materials. Hopkinson's law is defined as

$$\mathcal{F} = \Phi \mathcal{R} \quad (2.5)$$

where \mathcal{F} is the Magnetic Motive Force, \mathcal{R} is known as the reluctance of the material which the magnetic field is traveling through, and Φ is the magnetic flux. Each of these terms is analogous to a term in Ohm's law,

where the Magnetic Motive Force relates to the Electromotive Force, the magnetic flux to the current, and the reluctance to the resistance. In a circuit, a current will travel over all available paths, though the amount of current over each path is inversely proportional to the path's resistance. This is similar to magnetic fields, where the field permeates through all materials in the field's path, although the magnetic flux is inversely proportional to the reluctance of the material. This passive shielding effect can be seen in Figure 2.1, where the majority of the magnetic flux is traveling through the shielding material, with a reduced field in the shielded area.

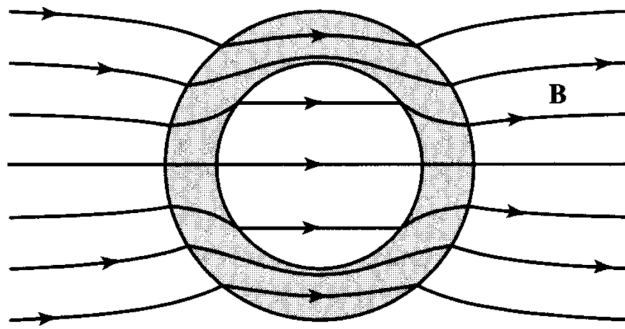


Figure 2.1: Example of magnetic field lines moving through magnetic shielding material. The majority of the field lines are passing through the shielding material, with a reduced field passing through the shielded area [4].

This reluctance of a material is related to its permeability. The permeability of free space is defined as $\mu_0 = 4\pi \times 10^{-7} \text{ m}\cdot\text{kg}/\text{s}^2\cdot\text{A}^2$, and is used for the permeability of any material with no magnetization properties. For materials that can be magnetized, its permeability is greater than the permeability of free space, and will thus be some multiple of μ_0 , with this multiple being defined as the relative permeability of the material, μ_r . This permeability is important for understanding the reluctance of the material, which can be calculated by

$$\mathcal{R} = \frac{l}{\mu_0 \mu_r A} = \frac{l}{\mu A} \quad (2.6)$$

where l is the length of the material, and A is its cross-sectional area. Following Equation (2.6), it can be seen that materials with the highest permeability have the lowest reluctance. However, as a condition of Hopkinson's law, the magnetic flux in a given material is inversely proportional to a material's reluctance, though proportional to its permeability. This means that materials with a larger permeability will have a larger flux concentration. Consequently, lower permeabilities correspond to a larger saturation limit, though

lower flux concentration. Various saturation limits and relative permeabilities for materials are tabulated in Table 2.1, where this relation can be seen.

Table 2.1: Relative permeabilities for various materials to show correlation between them. Values are maximum for each material at its saturation point where these values cannot increase anymore.

Material	Internal Saturation Field (G)	$\mu_r (\mu/\mu_0)$	Applied Field \mathbf{H} (Oe)
Metglas ^a	5,000	1,000,000	0.005
MuMetal (80% Ni) ^b	8,000	400,000	0.020
Iron (99.5% pure Fe) ^c	—	200,000	—
MuNickel (48% Ni) ^b	15,000	150,000	0.100
Iron (99.8% pure Fe) ^c	—	5,000	—
Low Carbon Steel ^b	22,000	4,000	5.500
Carbon Steel ^d	—	100	—

^a Reference [5]

^b Reference [6]

^c Reference [7]

^d Reference [8]

From this table, it's important to note that the relative permeabilities in the table are the maximum values which occur at the material's saturation limit since the permeability of the material changes as a function of the applied magnetic field, \mathbf{H} .

This \mathbf{H} is also known as the magnetic field strength, and is characterized as the magnetic field being applied to an object. The logic behind this term is for convenience since the magnetic field traveling through a material is different for all types of materials due to differences in permeabilities. This \mathbf{H} term makes comparisons of fields easier by removing this permeability dependence, and is especially useful when dealing with the reaction of magnetic materials to external fields. As a magnetic field permeates through a magnetic object, the magnetic material will also create an internal magnetic field itself, contributing to the overall field inside the material, making \mathbf{B} a non-linear function of \mathbf{H} . This magnetic field strength term allows for the ability to relate magnetic fields in different materials, and is defined by

$$\mathbf{H} = \frac{\mathbf{B}}{\mu} = \frac{\mathbf{B}}{\mu_0} - \mathbf{M} \quad (2.7)$$

where \mathbf{M} is defined as the magnetization of the object. The SI units for \mathbf{H} are Ampere–turns/meter (A/m), though for CGS it is the Oersted (Oe), where $1 \text{ A}/\text{m} = 0.01257 \text{ Oe}$. This relation is important because for non-magnetic materials, 1 Oersted is numerically equal to 1 Gauss since $\mu_r = 1$ [9]. The values of \mathbf{H} in Table 2.1 were calculated by dividing the internal saturation field by the relative permeability and is thus the

external magnetic field applied to the material in which its saturation limit is reached. Beyond this saturation limit, the number of field lines in the material cannot be increased with the externally applied field and would then behave as if the shielding material was not there.

2.2.2 MuMetal as a Passive Shield

In the lab there are unused MuMetal tubes, so they were tested to see if they would provide significant shielding for this project. These tubes were tested with a Gauss meter by measuring the magnetic field produced by a permanent magnet both with and without a MuMetal tube. Section 1.3 states that the NaI(Tl) array is located at a 12.65° angle from the center of the solenoid. As the radial component of the magnetic field is the most important, the permanent magnet was placed at approximately a 12° angle relative to the MuMetal tube to give the magnetic field a radial component. This would create similar conditions to that of the solenoid and would give an idea of whether the MuMetal tubes are a viable option as a passive shield. The dimensions of the shield used in these measurements can be found in Table 2.2.

Table 2.2: Dimensions of MuMetal Shielding being used

Characteristic	Value (cm)
Length	15.15
Outer Diameter	6.50
Inner Diameter	6.40
Material Thickness	0.10

For the first set of measurements, the B_z component of the magnetic field was measured for both cases with and without the MuMetal. These measurements were made from one end of the MuMetal tube to the other every 0.5 cm intervals, where the results for both with and without MuMetal can be seen in Figure 2.2. These results show that there is a significant reduction of the magnetic field with the MuMetal shield, with the most significant reduction occurring at about half the MuMetal length. Near the maximum shield length, the value of the magnetic field drops to zero, though a magnetic field was still present for the case without the MuMetal. This is a favorable result as the most sensitive part of the photomultiplier tubes is the end that is between the crystal and the first dynode. This is due to the fact that the initial photoelectron must cover a large distance when traveling to the first dynode, allowing for a smaller magnetic field to cause a much larger gain-shift. The results from this showed that for an initial z -component of ≈ 900 G, it was able to reduce it to less than 1 G near the end of the shield, which makes it ideal for the PMT's.

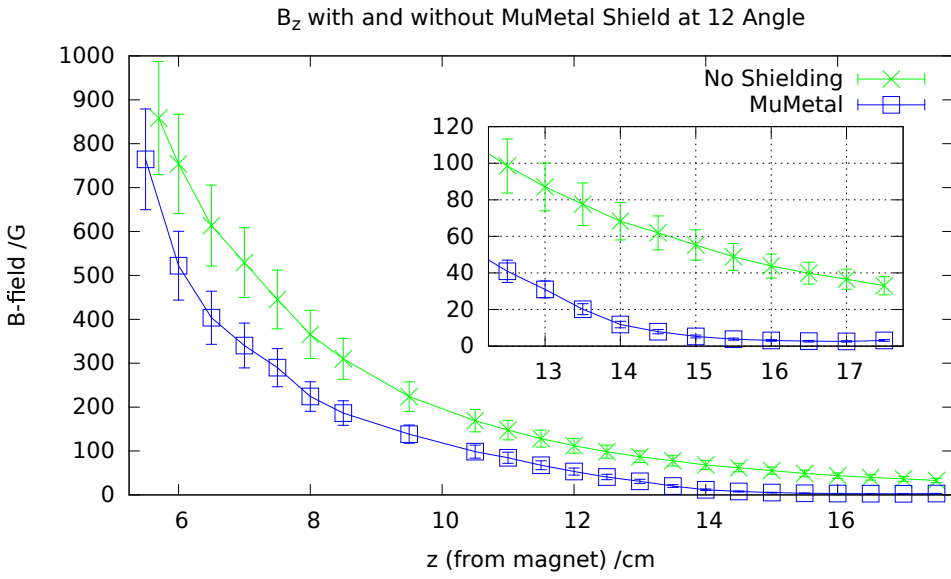


Figure 2.2: Test of how MuMetal shields from the z -component of the magnetic field.

This was repeated for the radial component case where the same procedure was followed with measurements being taken every 0.5 cm intervals. The results of these measurements can be found in Figure 2.3, where it can be easily seen that the MuMetal reduces the radial component of the magnetic field considerably. From a starting field of ≈ 120 G, the magnetic field in the MuMetal was reduced down to less than 1 G at the end. Again, the end of the PMT is the most sensitive to the magnetic fields, so this is ideal in preventing gain-shifting in the PMT's.

One final property that can be seen in both Figures 2.2 and 2.3 is how a magnetic material behaves under saturation and the effects this has on the shielded area. In the first few measurements for both B_z and B_r , the value of the magnetic field decreases at the same rate in both the shielded and unshielded cases. This trend continues in both measurements until an external z -component of approximately 50 G and a radial component of approximately 10 G is achieved, at which point the shielded region drops to less than 1 G. From these measurements, the ideal goal will be to get the magnetic field from the solenoid down to a maximum of 50 G at the location of the PMT's, from which the MuMetal shield can bring the residual field down to appropriate levels.

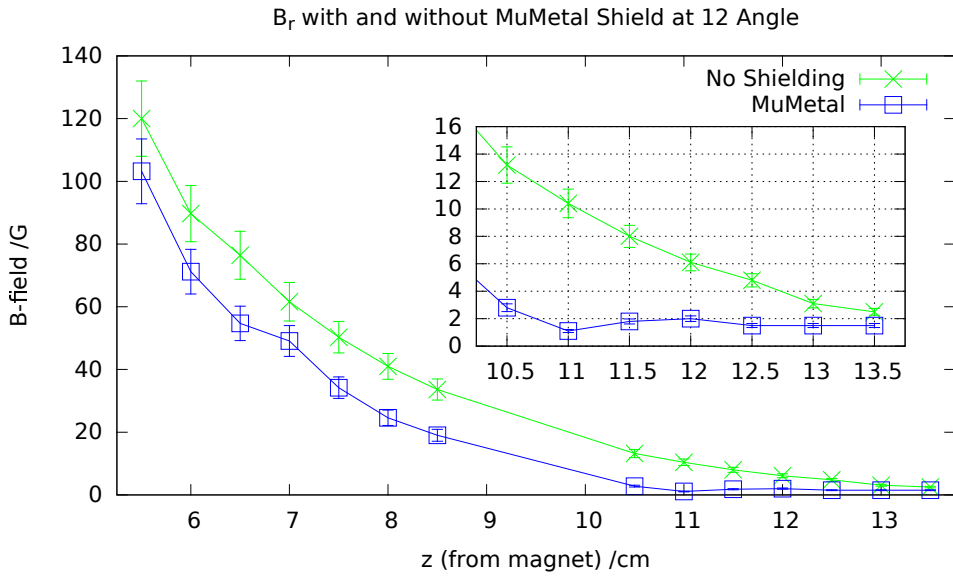


Figure 2.3: Test of how MuMetal shields from the radial component of the magnetic field.

2.2.3 Effects of Mechanical Stress on MuMetal

When researching the physical properties of shielding materials, various sources mentioned the possibility of problems arising when cutting or severely stressing the material [10, 11]. Due to the dimensions of the MuMetal and the PMT's, the MuMetal must be cut along the longitudinal and bent around the PMT to fit on it, so this was an important factor to test.

The same procedure was followed as in the previous section, with the only difference being that the measuring interval was every 1 cm instead of every 0.5 cm. For these measurements, there is one important factor which must be mentioned as it influences the results. In the group of MuMetal tubes, there was one tube that had already been stressed by being cut short by a few centimeters. As the influence of stressing a MuMetal tube was unknown, and wasting a MuMetal tube was not desired, this shortened tube was the one chosen to be cut and bent for the stress testing. That way, if the shielding properties of the MuMetal significantly decreased, a fully functional MuMetal tube would not be wasted and an alternative method to mount the MuMetal to the PMT's could be found. However, since a shorter tube was used, this caused the magnetic field at the last location to be greater than in the case of the unstressed tube.

The results for these tests can be found in Figure 2.4 for the z -component, and Figure 2.5 for the radial component. In these results, it can easily be seen that any adverse effects from this cutting and stressing

process is negligible. At the end of the PMT's, the magnetic field in the stressed MuMetal is higher than in the non-stressed case as it was cut shorter. Ill effects imposed into the shielding material are not required and this absence of a difference between the two can be attributed to the fact that modern day vacuum-refined alloys have a lower sensitivity to mechanical shock [12]. It was unknown if this was the case for the MuMetal tubes that were being used, so this was an important factor to test.

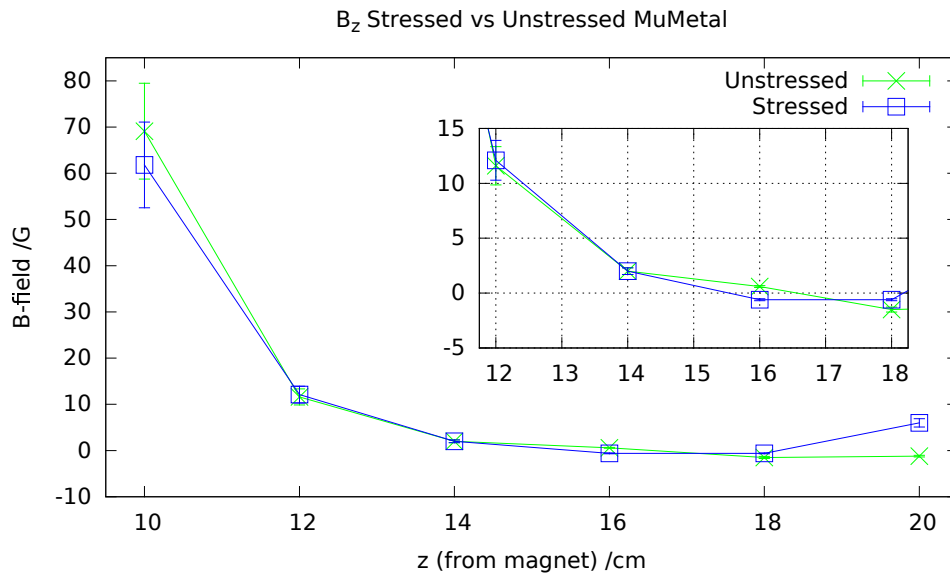


Figure 2.4: Testing the abilities of shielding from the z -component after being stressed and cut.

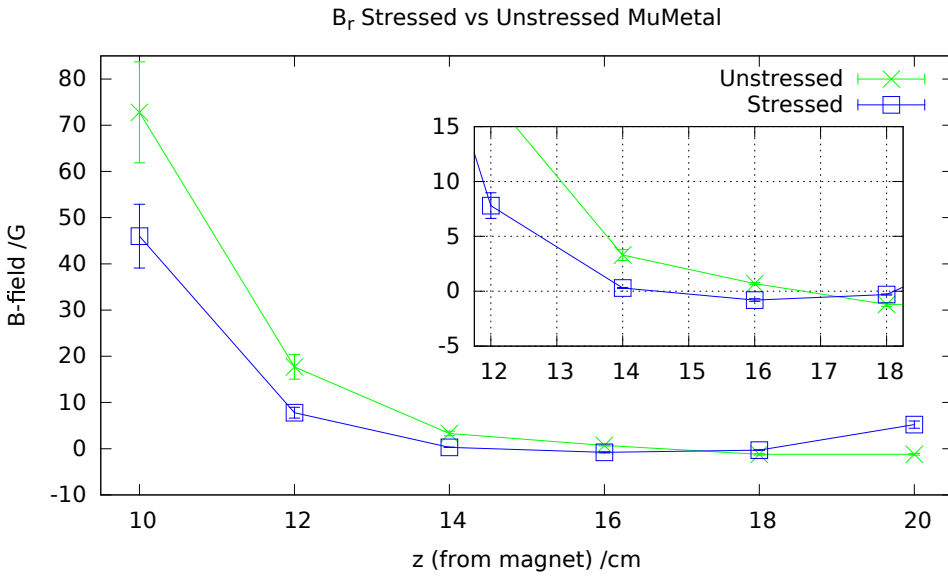


Figure 2.5: Testing the abilities of shielding from the radial component after being stressed and cut.

2.2.4 Active Shielding

Active shielding falls under the principle of constantly applying an opposing magnetic field to a given area to cancel the magnetic field, where the most common types of active shields are solenoids and Helmholtz coils. These are the most common because creating a constant, homogeneous, magnetic field can be easily achieved. For the purpose of this project, the Helmholtz coil was chosen due to the fact that it can be easily placed around the array of PMTs, and having more freedom in adjusting the magnetic field it produces. For example, if a radial component of the residual field needs to be canceled, a radial component in the field produced by the Helmholtz coil can be produced by simply using asymmetric currents.

As stated in Section 1.3, the radius of the array of NaI(Tl) detectors is 0.20 meters. Therefore, the Helmholtz coil must be slightly larger than this, as such a radius of 0.25 meters was chosen. The equation for the magnetic field that a Helmholtz coil produces at its center can be found below, with the derivation of the equation being found in Appendix B.

$$\mathbf{B} = \frac{8\mu_0 NI}{5^{3/2}R} \hat{k} \quad (2.8)$$

Where N is the number of turns in one Helmholtz coil, I is the current flowing through the coil, and R is the radius of the coil. By simply rearranging this equation, the amount of current required for canceling a

magnetic field of a certain magnitude can be obtained. By performing these algebraic operations, the resulting equation for the current in the Helmholtz coil is

$$I = \frac{BR5^{3/2}}{8\mu_0 N} \quad (2.9)$$

Another factor to take into consideration for the Helmholtz coil is the amount of power output in the form of resistance in the coil wire. With too high of a power output, problems may arise such as the melting of the wire insulation or the wires fusing together. The power output from the resistance in the wire can be calculated with Equation (2.10).

$$P = I^2 R \quad (2.10)$$

Where P is the power output in Watts (W) and R is the natural resistance that the wire produces in Ohms (Ω). The resistance in the wire can be calculated via

$$R = \frac{\rho L}{A} \quad (2.11)$$

where ρ is the resistivity of the material, $1.68 \times 10^{-8} \Omega \cdot \text{m}$ for Copper at 20°C , L is the length of the wire, and A is the wire's cross-sectional area. An ideal case would be for the coil's power output to be less than 100 W, as that is the power output of a standard incandescent light bulb, thus requiring no cooling. After determining the current needed to cancel the magnetic field down to appropriate levels, a simple program can be used to iterate through different wire gauges to see which one meets these requirements. The source code for this program can be found in Appendix B.

2.3 Simulating the Magnetic Field

As stated at the beginning of Section 2.1, direct measurements of the magnetic field cannot be made accurately and must be calculated instead. The simulation was created in C++, and was used for calculating the magnetic field for both the solenoid and the Helmholtz coil as it was used for an active shield. For the simulation, each loop of the solenoid and Helmholtz coil was approximated to be an individual coil with a uniform current passing through it. The source code for this simulation can be found in Appendix B.

The company that manufactured the solenoid provided documentation that stated only some of the dimensions of the solenoid, with two major unknown parameters being the solenoid's length and the number

of turns. Along with the given parameters, included was a table of calculations of the on-axis magnetic field that the solenoid produces.

To determine the length of the solenoid, the dimensions of the cryostat was provided so the length was approximated to be 10 cm shorter on each end of the solenoid in relation to the cryostat. To approximate the number of turns, the on axis magnetic field was calculated with an arbitrary number of turns and then varied until the magnetic field inside the solenoid matched the calculations provided by the manufacturer.

One final important parameter was the dimensions of the wire used for the solenoid, as each successive coil loop varies both the radius and distance between the point at which the magnetic field is being calculated changes based on the radius of the wire. Once the number of turns was determined by using the previously stated method, the solenoid's volume was divided by this number to determine the approximate volume dimensions of each coil in the solenoid. From here, the radius of the wire could be determined. This calculation is hard-coded into the simulation so that the wire dimensions in the solenoid can vary as a function of the number of turns. All of the other values that were necessary for the simulation were given by the manufacturer and can be found in Table 2.3.

Table 2.3: Values for Simulating Solenoid

Characteristic	Value
Length	0.63 m [†]
Max Current	139.2 A
Minimum Radius	0.14224 m
Maximum Radius	0.20320 m
Number of Coils	228,010 [†]
Number of Layers	33 [†]

[†] Denotes estimated or free parameter

Table 2.4: Values for Simulating Helmholtz Coils

Characteristic	Value
Radius	0.25 m
Wire Gauge/Diam.	9/0.002906 m
Number of Coils	50
Number of Coil Layers	5
Current for closest coil	-40 A
Current for furthest coil	-50 A

As can be seen in Figure 2.6, the simulation accurately depicts the magnetic field of a solenoid based on the vector field. The black boxes in the figure indicate the dimensions of the solenoid where the coils were located. By following the field lines, the magnetic field can be seen to be constant along the z -component inside the solenoid, and curve around after leaving the solenoid's center. The magnitude of the solenoid was also calculated and can be seen in Figure 2.7.

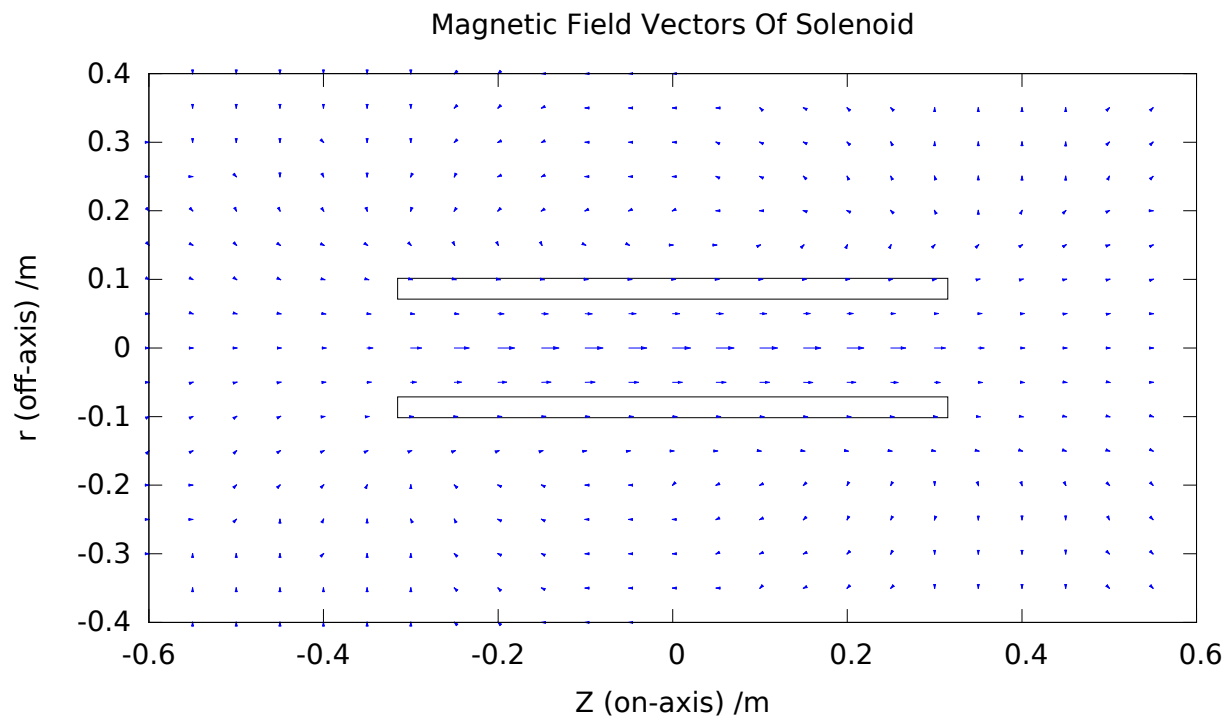


Figure 2.6: Figure of the calculated Magnetic Field lines from the solenoid.

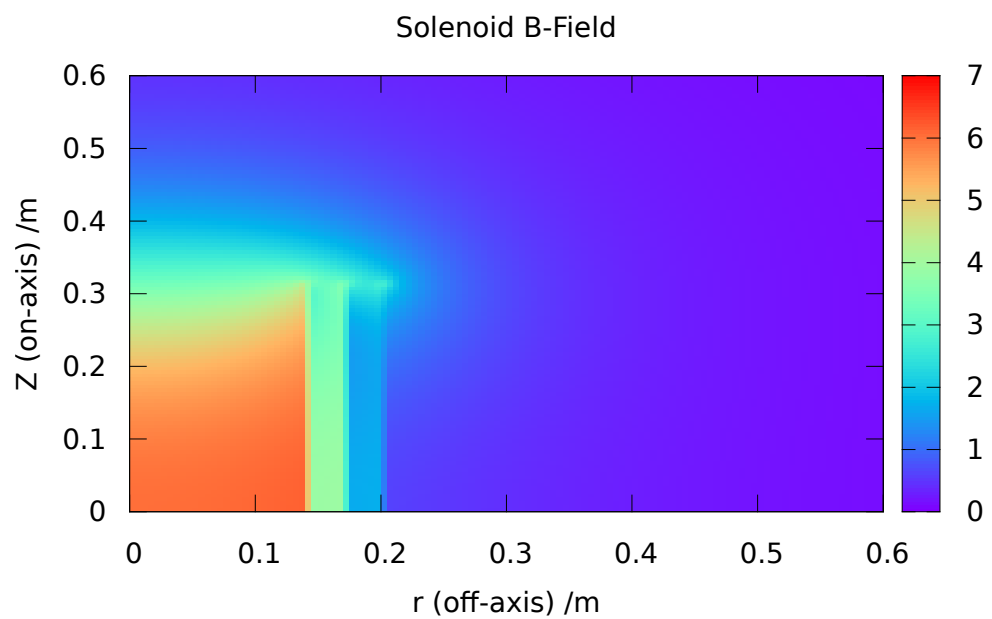


Figure 2.7: Figure of the calculated magnitude of the magnetic field.

This figure contains result that appropriately describe what is to be expected for the magnitude of the magnetic field being produced in a solenoid, with the maximum values being located at the center of the solenoid and the magnitude decreasing away from the solenoid's center. The change in the magnetic flux permeating through each layer of coils decreases as well which follows what is to be expected. With each progressive layer, there are fewer layers contributing to the magnetic field at the coil location which causes the decrease in flux.

Finally, the simulation can be compared to the calculations given by the manufacturer, as found in Figure 2.8. In this figure, the values from the simulation agree with the calculations provided by the manufacturer, where the smaller plot is the on-axis location of where the PMT's are located so verifying the accuracy here is crucial for running later calculations. While both results do agree with one another, the simulation produces values which are slightly higher than the calculations provided by the manufacturer, where this difference can be attributed to the manufacturer having better knowledge of the solenoid's dimensions.

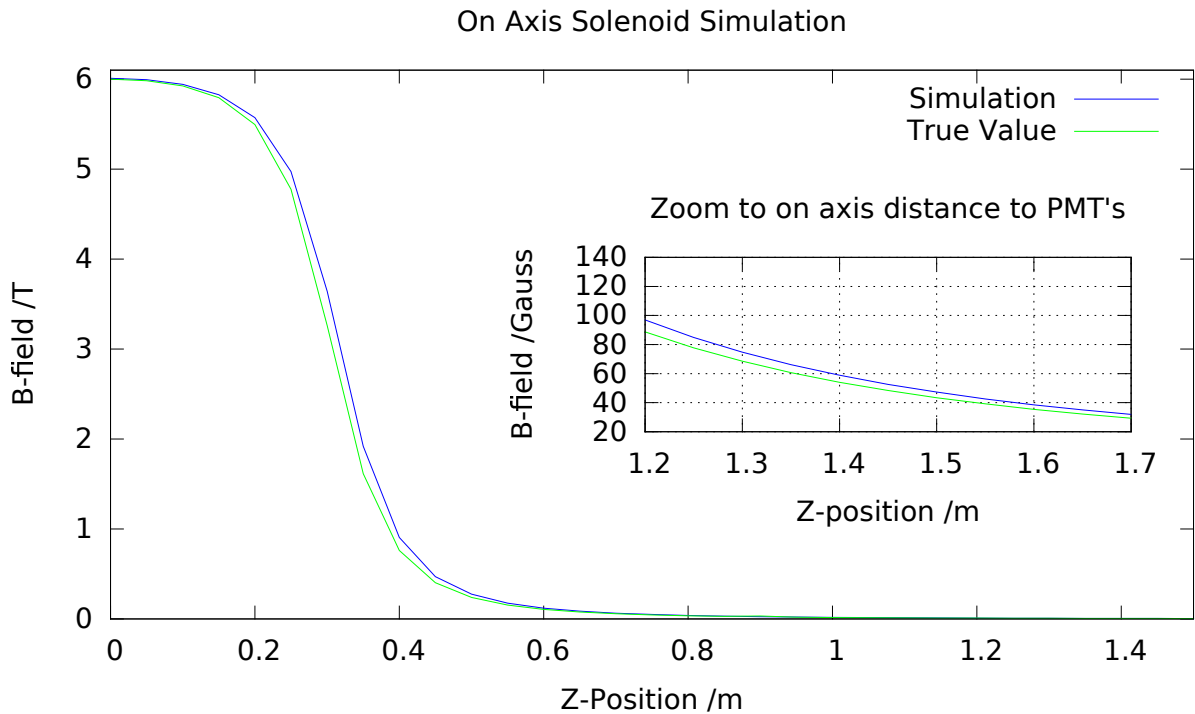


Figure 2.8: Simulation vs Measured vs Manufacturer values.

As the simulation is essentially only using Equations (2.2), (2.3), and (2.4) from the Biot-Savart law, it can easily be adapted to calculate the magnetic field produced by the Helmholtz Coil as well. This can

be seen in Figure 2.9, where the black boxes denote the geometry of the Helmholtz coil. By looking at the direction of the magnetic field lines, and comparing it to what is expected for a Helmholtz coil, this simulation successfully recreates the appropriate magnetic field for this case as well. From these successful simple cases, the conclusion can be made that the simulation works well for these values.

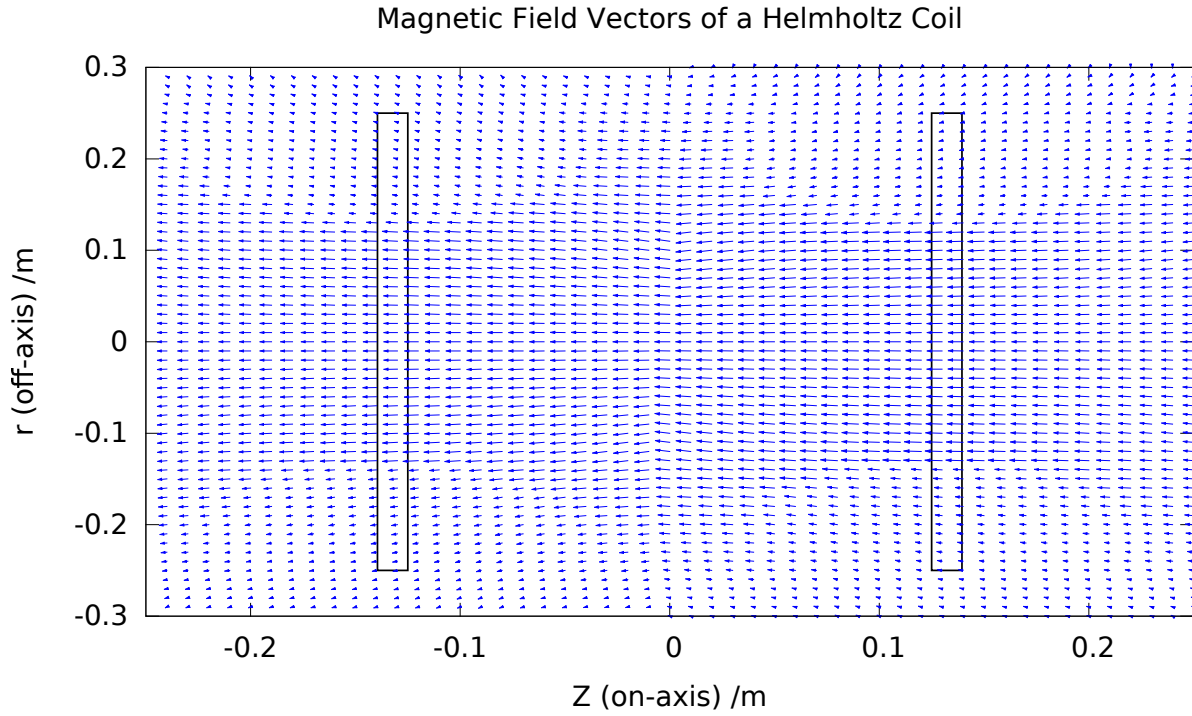


Figure 2.9: Simulation of Helmholtz Coil.

2.3.1 Numerical Integration Technique

Initial attempts at running the simulation took a substantial amount of time, with a calculation of just the magnetic field at locations around the solenoid taking on the order of two weeks of CPU time for high position resolution. To speed up the calculations, a numerical technique known as the adaptive quadrature method was implemented into the simulation to provide the numerical integration values.

This method is based on Simpson's Rule of numerical integral approximation which takes a given interval and samples values of the function over equal intervals and uses these values to approximate the integral. This method is well suited for trigonometric functions due to their cyclic nature. The adaptive quadrature method follows this same principle, with the difference residing in the interval between the number of points. This method does not sample the number of points over equal intervals, but rather varies the difference between

the sampling points based on the slope of the function, where parts of the function with a greater slope have points which are less spaced out due to the large changes in the functional values. Figure 2.10 is a graphical depiction of how this method works.

Since Equations (2.2), (2.3), and (2.4) are the ones integrated, and they are composed of trigonometric functions, this method performs well in integrating these. Alongside the fact that it is composed of trigonometric functions, the variable distance between the number of points greatly reduced the number of required computations, resulting in a factor of 100 less computations for each integral performed with no loss in accuracy.

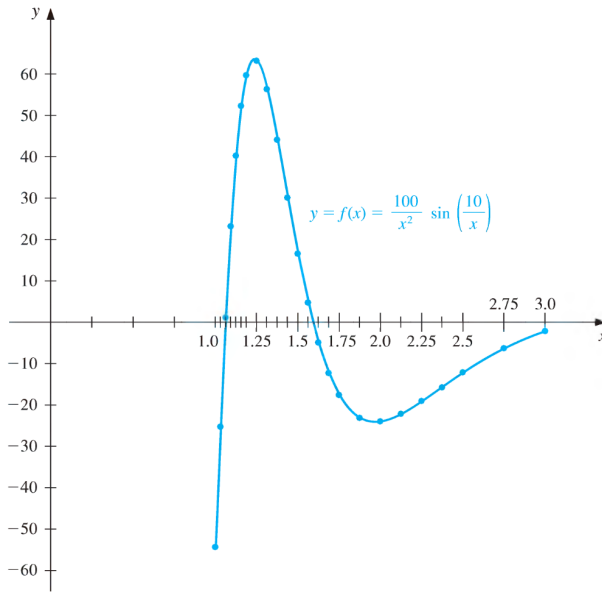


Figure 2.10: Graphical depiction of how the Adaptive Quadrature Method works [13].

CHAPTER 3

RESULTS

3.1 Magnetic Field from the Solenoid

The simulation of the solenoid allows the values of B_z and B_r to be obtained over various coordinate positions, specifically at the location of the PMT's. The values used for this simulation are located in Table 2.3, where the current used was the maximum allowable current in the solenoid to test the limiting case. If the magnetic field can be reduced enough for this case, then it can easily be reduced under normal operating conditions which is with a current of 50 Amps.

Figure 3.1 shows the result of the simulation, with the black boxes defining the Helmholtz coil location and dimensions, and the red boxes denoting the location of the PMT's by using the dimensions of the MuMetal tube. In this figure, it can easily be seen that there is a large radial component in this field which would cause significant gain-shifting in the newer Hamamatsu R2154 PMT's. The values of the magnetic field at these locations have a maximum z -component of 70 Gauss, and a maximum radial component of 20 Gauss. This is the field that has to be canceled by both the Helmholtz coil and the MuMetal shield.

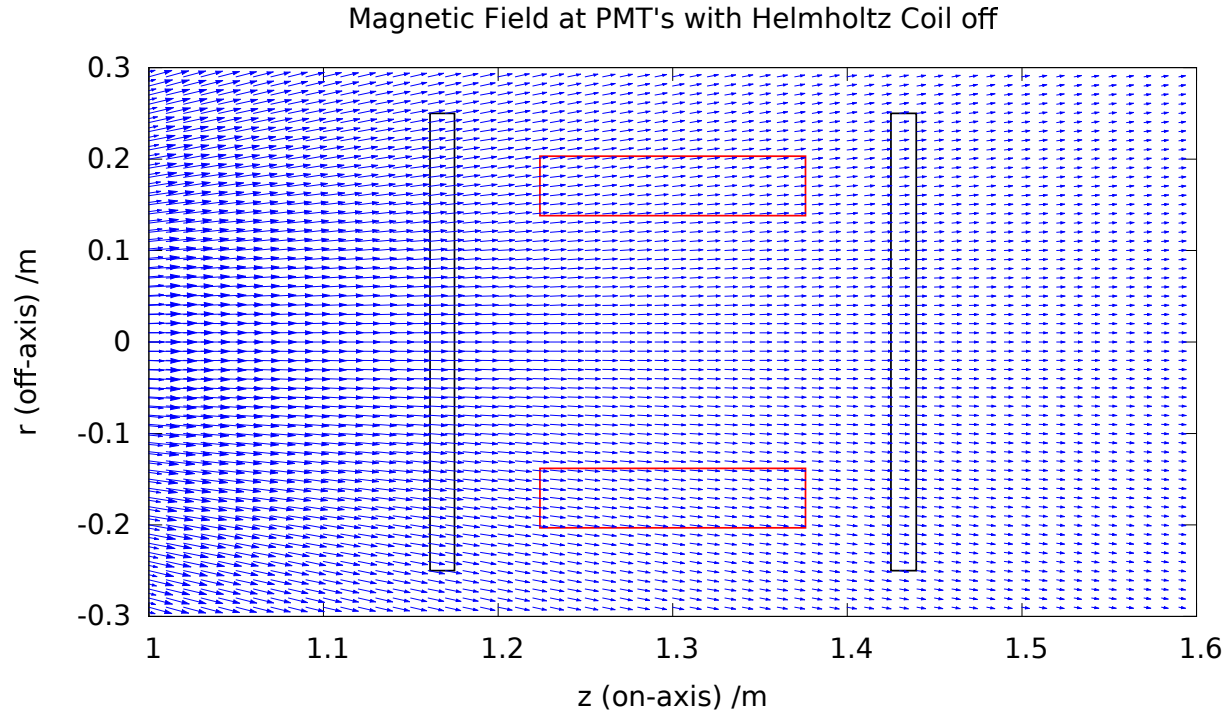


Figure 3.1: Magnetic field of the solenoid at the location of the PMT's.

3.1.1 Active Shielding with a Helmholtz Coil

In order to cancel the magnetic field with a Helmholtz coil, the current required to cancel out a 70 Gauss z -component magnetic field was obtained via using Equation (2.9). This resulted in a required current for a single-loop Helmholtz coil being 2,000 Amps. Since the current in a Helmholtz coil scales inversely as a factor of the number of loops, the number of loops for the Helmholtz coil was obtained by choosing a number that was not excessive, though gave a realistic value for the current. The decision for this was a Helmholtz coil with 50 loops, resulting in a current of only 40 Amps being required to reduce the field. These 50 loops are distributed such that there are 5 layers of 10 coils along the axis. In order to produce a magnetic field that opposes that of the solenoid, the current through the Helmholtz coil needs to travel in the opposite direction of the solenoid's current. As the current in the solenoid was defined as positive, in order to cancel the field the resultant current would thus be -40 Amps.

This -40 Amps of current is what is used for producing a uniform magnetic field, though as seen in Figure 3.1, the magnetic field at the location of the PMT's contains a radial component. In order to give the magnetic field in the Helmholtz coil a radial component to cancel the field, the current through each of

the coils was made asymmetric. The optimal combination of currents was determined by running various simulations with different current combinations. In the calculations of the magnetic field in Figure 3.1, the direction of the radial component is positive, meaning the coil closest to the solenoid must carry a current that is larger than the one furthest from the solenoid to produce a negative radial component between the coils. From these trials, the ideal situation was with a current of -50 Amps traveling through this half of the Helmholtz coil.

With the required current determined, the amount of heat that the Helmholtz coil would produce for various wire dimensions was calculated. The ideal case was to decide on a wire gauge such that the Helmholtz coil would produce less than 100 W of power output, thus requiring no cooling. This was done with Equation (2.11) over various wire gauges leading to the result of a 9 gauge wire, with a diameter of 2.906 mm, producing approximately 80 W of heat dissipation. This falls within the given constraints and is used in all subsequent calculations. All parameters that were used in simulating the Helmholtz coil can be found in Table 2.4, with the simulation results being in Figure 3.2.

After running this simulation, the maximum residual magnetic field occurred at the outer edges of the MuMetal at the end closest to the solenoid, with a resulting maximum field of 27 G B_z component, and a 10 G B_r component. The minimum residual field was located at the inner section of the MuMetal tube with a field of 13 G and 4 G for the B_z and B_r components, respectively. At these levels, the MuMetal shielding needs to lower the magnetic field to appropriate levels for the R2154 PMT's to function properly.

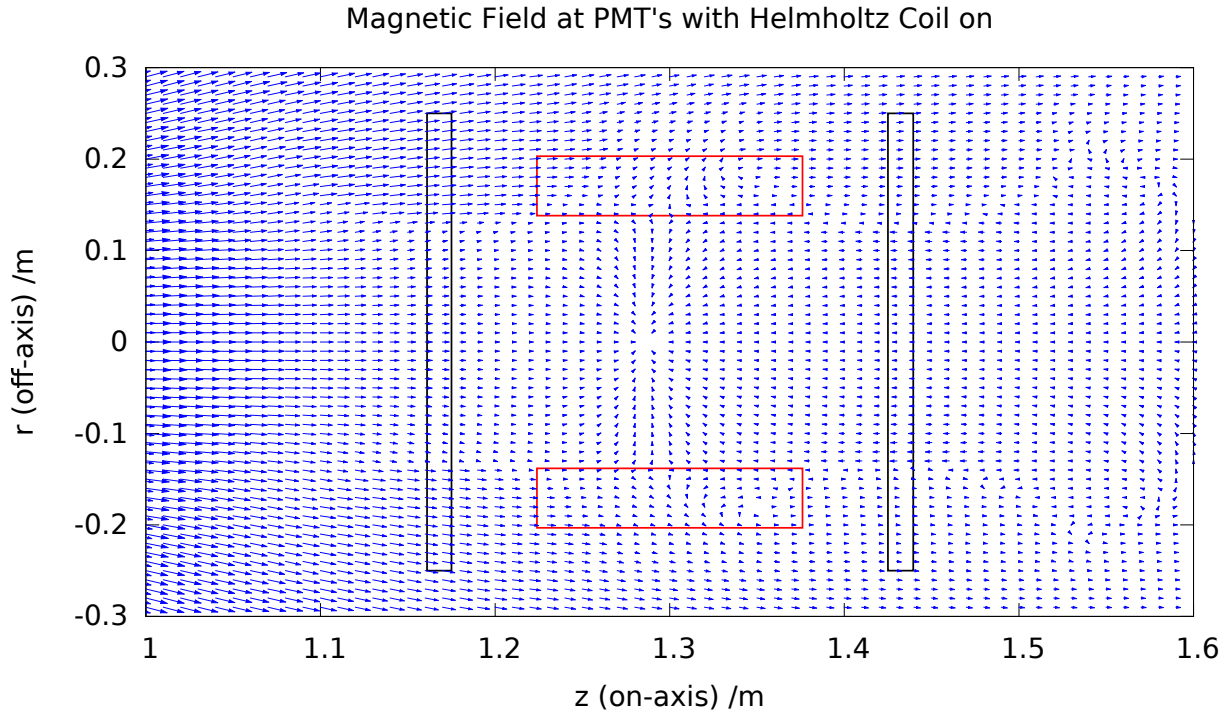


Figure 3.2: Residual Field of the solenoid after turning on the Helmholtz Coil to cancel the field.

3.1.2 Passive Shielding with MuMetal

Simulating the exact values inside shielding materials requires solving a non-linear Partial Differential Equation. This is extremely computationally intensive, though other calculations can be performed to provide a good approximation of the shielding results. Along with re-analyzing the measurements from Section 2.2.2, three different calculations are performed to determine the effectiveness of the MuMetal tubes, and the dimensions of the MuMetal tubes are found in Table 2.2.

The results of the measurements in Section 2.2.2 are able to experimentally determine how effective the shielding material will be. In Figures 2.2 and 2.3, the magnetic field inside of the MuMetal tubes drops to essentially zero for an external field composed of 50 G B_z component and a B_r component of 11 G. From the simulation, the maximum magnetic field that the MuMetal tubes will experience is one with a 27 G z -component and 10 G radial component. The Gauss meter used is not sensitive enough to accurately measure below 1 G, though these measurements are good for a first order approximation and show that the MuMetal shielding would be effective in reducing the magnetic field. In order to be more certain, three different calculations to verify these results are made below.

For the first set of calculations, there is data which contains measurements dealing with determining the magnetic field inside shielding materials that used much more precise instruments. The results provide a ratio of the magnetic field inside and outside of the shield based on the relative thickness of the material. The results from these measurements were obtained from [14] and the ratio can be used to approximate the maximum field that will be seen inside the MuMetal. By calculating the ratio of the thickness of the MuMetal (R_{in}/R_{out}) from the values in Table 2.2, the result is a ratio of 0.985. As stated in the previous section, the field that the MuMetal needs to cancel out is 10 Gauss radial and 27 Gauss z -component.

Figure 3.3 shows these results used to calculate the aforementioned ratio (B_{in}/B_{ext}). By using this figure, the 1 mT (10 Gauss) curve corresponds to $\frac{R_{in}}{R_{out}} = .973$, and a magnetic field ratio of $\frac{B_{in}}{B_{ext}} \approx \frac{1}{900}$. By applying this ratio to an external field of 10 Gauss, the result would be an internal magnetic field on the order of 0.01 Gauss, which is within the threshold required for optimal operation of the new PMT's. However, this is for a shield with a thickness ratio of 0.973, whereas the ratio of the MuMetal tubes being used is 0.985, meaning the residual field in the actual shield being used should be less than 0.01 Gauss.

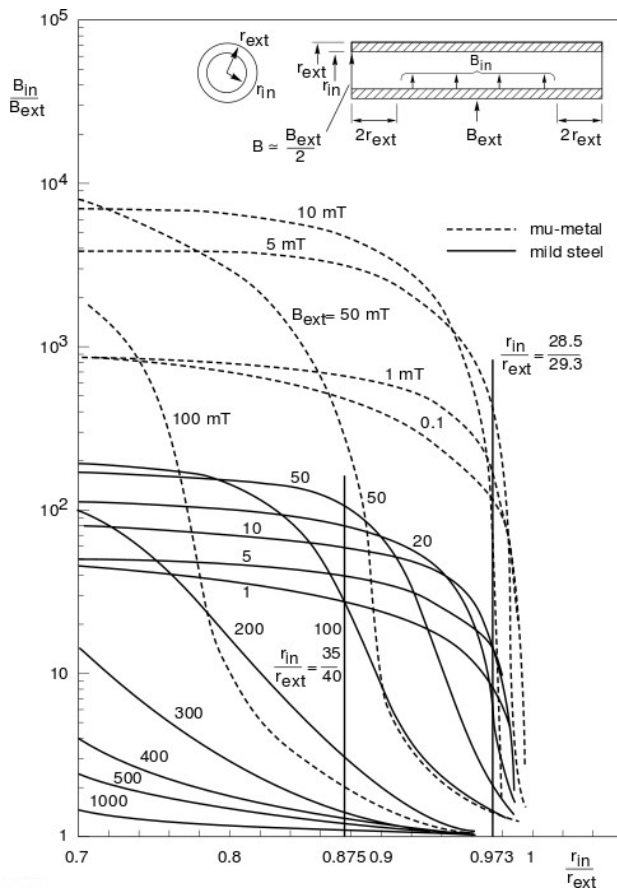


Figure 3.3: Figure showing measurements of the ratio of the external magnetic field to the internal magnetic field as a function of the shielding material thickness [14].

An alternative way of checking the shielding effectiveness is to calculate the amount of magnetic flux that travels in through the MuMetal and the shielded region. The magnetic flux is proportional to the number of magnetic field lines passing through a given cross-sectional area, meaning a larger flux in the MuMetal would correspond to at least partial shielding occurring in the shielded region. Figure 3.4 shows the cross-sectional area that is to be calculated for each given region.

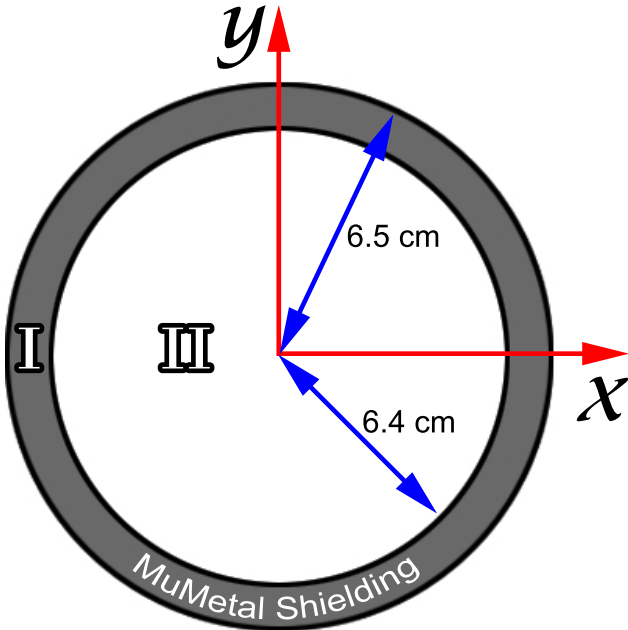


Figure 3.4: Diagram of the cross-sectional area of the MuMetal Shield.

In order to be able to calculate this flux, the magnetic field inside the MuMetal needs to be known. The MuMetal material is from Magnetic Shield Corp., and they provide a B-H Curve for the various magnetic shielding materials which they sell. This B-H Curve shows the value of the internal magnetic field for various applied fields, along with the permeability of the material in these situations. Figure 3.5 shows these values, where the applied field can be taken to be 20 Oersteds, or the equivalent of 20 Gauss. This is past the saturation point of this material, so the magnetic field inside of the MuMetal would correspond to an internal field of 0.8 Tesla.

With these values, the flux for both regions can easily be calculated since the flux is simply the amount of magnetic field traveling through a given area, where the equation for the magnetic flux in SI units is then

$$\Phi_B = \iint_S \mathbf{B} \cdot d\mathbf{S} \quad (3.1)$$

Where Φ_B is the amount of flux within a given area S in units of Weber (Wb), and \mathbf{B} is the magnetic field in the region in units of Tesla (T). Due to the simple geometry of the given situation, it can be reduced down to simply the magnetic field in a given region times the area of the region in question. This results in the flux of the two regions as defined in Figure 3.4 being

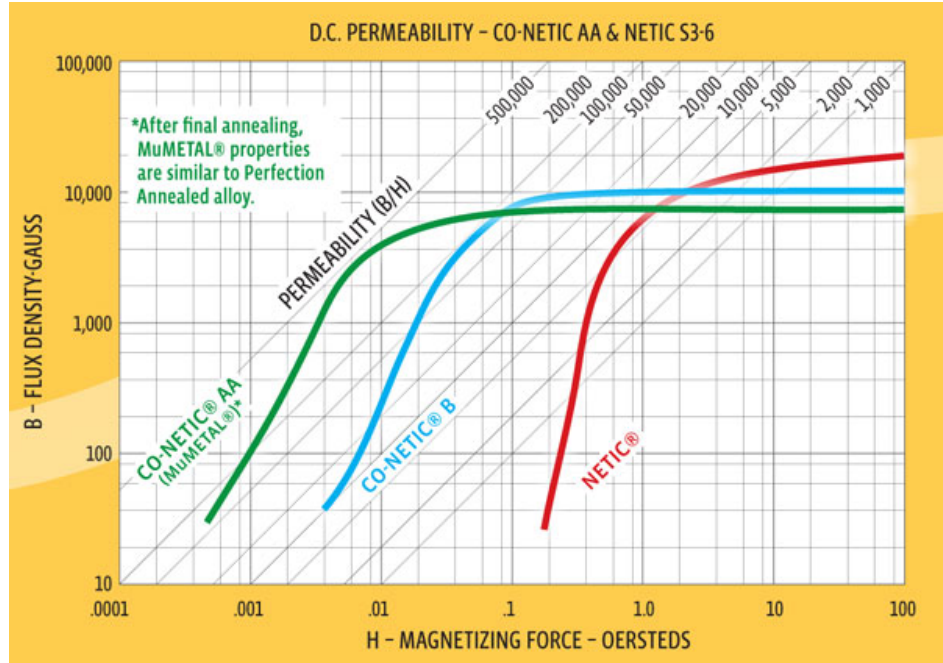


Figure 3.5: B-H Curve for various shielding materials provided by Magnetic Shielding Corp. [15].

Region I

$$\Phi_\mu = \mathbf{B}_\mu \cdot \mathbf{A}_\mu$$

$$\Phi_\mu = 0.8 \text{ T} (r_2^2 - r_1^2) \pi$$

$$\Phi_\mu = 0.8 \text{ T} (0.065^2 \text{ m}^2 - 0.064^2 \text{ m}^2) \pi$$

$$\Phi_\mu = 3.24 \times 10^{-4} \text{ Wb}$$

$$\Phi_\mu = 32,400 \text{ Maxwell } (\text{Gauss} \cdot \text{cm}^2)$$

Region II

$$\Phi_{in} = \mathbf{B}_{in} \cdot \mathbf{A}_{in}$$

$$\Phi_{in} = \frac{20 \text{ G}}{10,000} (0.064 \text{ m})^2 \pi$$

$$\Phi_{in} = 0.002 \text{ T} (0.064 \text{ m})^2 \pi$$

$$\Phi_{in} = 2.6 \times 10^{-5} \text{ Wb}$$

$$\Phi_{in} = 2,600 \text{ Maxwell } (\text{Gauss} \cdot \text{cm}^2)$$

These results show a larger magnetic flux passing through the MuMetal (Region I) when compared to the shielded area (Region II), even though the applied field is beyond the saturation limit. These results lead to the conclusion that the magnetic field will be reduced in Region II as the majority of the magnetic flux will be contained in Region I.

Finally, there is one last calculation for the effectiveness of the MuMetal shield. The manufacturer of the MuMetal, Magnetic Shield Corp., provides an online calculator based on experimental results that they've obtained over the years. This program is used for approximating the reduced field for various thicknesses of materials to give customers an idea of the shielding dimensions they require. Table 3.1 shows both the input and output from this calculator, with the attenuation factor being the ratio between the applied field to the reduced field. Magnetic Shield Corp. is a North American based company and thus uses imperial units for length measurements, so these values have been converted into centimeters for convenience.

From this table, the magnetic field corresponding to the dimensions of the MuMetal tubes being used corresponds to a reduced field of 0.0041 Gauss, with an attenuation factor of 4878. Figure 1.6 shows how the sensitivity of the R2154 PMT's change as a function of \mathbf{H} , where the goal was to reduce the field down to less than 0.5 A/m, 0.00628 G, to maintain optimum operating conditions. The results from the calculations shows the reduced field would be less than this, meaning that the PMT's will be in a favorable field.

Table 3.1: Calculation of residual field in the MuMetal for various shielding thicknesses [16]. FTH denotes when the calculated residual field in the shielded region was too high.

Input		Output		
Shield Diam. (cm/in)	H_0 (Gauss)	Shield Thickness (cm/in)	Attenuation	B_s (Gauss)
6.5/2.56	20	0.0051/0.002	FTH	
6.5/2.56	20	0.0102/0.004	FTH	
6.5/2.56	20	0.0152/0.006	FTH	
6.5/2.56	20	0.0203/0.008	FTH	
6.5/2.56	20	0.0254/0.010	FTH	
6.5/2.56	20	0.0356/0.014	FTH	
6.5/2.56	20	0.0508/0.020	3654	0.0055
6.5/2.56	20	0.0635/0.025	4186	0.0048
6.5/2.56	20	0.0762/0.030	4471	0.0045
6.5/2.56	20	0.1016/0.040	4878	0.0041
6.5/2.56	20	0.1270/0.050	5304	0.0038
6.5/2.56	20	0.1575/0.062	5888	0.0034

3.2 Conclusion

In order to use the Hamamatsu R2154 PMT's with the NaI(Tl) array, the magnetic field at their location had to be canceled. These detectors have a much higher resolution than the currently installed Hamamatsu H2611 PMT's, though are much more sensitive to magnetic fields.

Doing so required knowing the exact values of the magnetic field, both the longitudinal and lateral components. To achieve this, a simulation of the solenoid was created and used for these values. These results could then be used in determining the optimum approach to cancel the magnetic field at the location of the PMT's. The simulation stated a maximum magnetic field of 70 Gauss longitudinal and 20 Gauss lateral.

The best course of action was to utilize the shielding properties of both a passive and active magnetic shield. The active shield of choice was a 0.25 meter radius Helmholtz coil with the use of asymmetric currents. These asymmetric currents produced a field which was non-homogeneous and gave the field a radial component. This was done since the PMT was most sensitive to radial magnetic fields and caused the largest problems. With the use of a -50 Amp and -40 Amp currents, this radial component was able to be reduced down to approximately 10 Gauss. Under operation, the resistance in the coil would cause an output of heat – so for performance purposes this had to be considered as well. The ideal situation was a power output of less than 100 Watts, as no type cooling would be required. This was determined to be achievable with a 9 Gauge wire which has a diameter of 0.002906 meters.

This then had to be finally reduced with a passive shield, which the passive shield that was used was a 6.5 cm diameter MuMetal tube which has a thickness of 0.1 cm. Exact calculations could not be made, though all approximations in the shielding effectiveness lead to the result of the field being reduced to appropriate levels.

One of these approximations was based on measurements provided by an engineering company which lead to the conclusion that the internal magnetic field would be less than 0.01 Gauss. The other was a calculation on the flux in each of the regions, which lead to 32,400 Maxwell and 2,600 Maxwell in the MuMetal and shielded region, respectively. This meant that the majority of the magnetic field would be contained in the shield and not in the shielded region. Finally, the shields were manufactured by Magnetic Shield Corp., and they provide an online calculator to approximate the field for various materials which they sell. The results from this stated that the internal magnetic field would be reduced to 0.0041 Gauss. The overall goal was to bring the field down to less than 0.5 A/m (0.0063 Gauss), which these results show was achieved.

APPENDIX A

DERIVATIONS

A.1 Off-Axis Biot-Savart Equations

The beginning of this starts off with Equation (2.1), the Biot-Savart Law. In Figure A.1, all of the variables that are used for this derivation can be found. As the coils move throughout the solenoid, a generalized version of this equation is

$$\mathbf{B} = \frac{\mu_0 I}{4\pi} \int_C \frac{d\ell \times (\mathbf{r} - \mathbf{r}_c)}{|\mathbf{r} - \mathbf{r}_c|^3} \quad (\text{A.1})$$

where \mathbf{r} is the vector to the point in question, and \mathbf{r}_c is the position of the coil. As this is being done for a solenoid, the \mathbf{r}_c value varies throughout the calculations, starting at zero and increasing along the length of the solenoid.

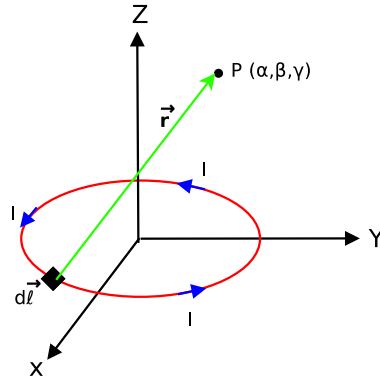


Figure A.1: Diagram of a single loop which is used for all of the loops in the simulation.

The simplest approach for this would be in cylindrical coordinates, where the conversion between the two coordinate systems is defined by:

$$\begin{aligned} x &= R \cos \theta \\ y &= R \sin \theta \\ z &= z \end{aligned}$$

where R is the radius of the coil, and θ is the contour around the coil, ranging from 0 to 2π . In Figure A.1, $d\ell$ is the differential current element following this contour. From this, the following vectors can be obtained

$$\begin{aligned}
\mathbf{r} &= \alpha \hat{i} + \beta \hat{j} + \gamma \hat{k} \\
\mathbf{r}_c &= R \cos(\theta) \hat{i} + R \sin(\theta) \hat{j} + z \hat{k} \\
\boldsymbol{\ell} &= R \cos(\theta) \hat{i} + R \sin(\theta) \hat{j} + z \hat{k} \\
d\boldsymbol{\ell} &= -R \sin(\theta) \hat{i} d\theta + R \cos(\theta) \hat{j} d\theta + 0 \hat{k}
\end{aligned}$$

With using these vectors, the cross product from Equation (A.1) can be taken, with the result being

$$\begin{aligned}
d\boldsymbol{\ell} \times (\mathbf{r} - \mathbf{r}_c) &= \begin{vmatrix} \hat{i} & \hat{j} & \hat{k} \\ -R \sin(\theta) d\theta & R \cos(\theta) d\theta & 0 \\ \alpha - R \cos(\theta) & \beta - R \sin(\theta) & \gamma - z_c \end{vmatrix} \\
&= (\gamma - z_c) R \cos(\theta) \hat{i} d\theta + (\gamma - z_c) R \sin(\theta) \hat{j} d\theta + R(R - (\alpha \cos(\theta) + \beta \sin(\theta))) \hat{k} d\theta
\end{aligned}$$

These individual components can be taken and plugged into the Biot-Savart law to get the the following equations for the components of the magnetic field

$$B_x = R_0 \frac{\mu_0 I (\gamma - z_c)}{4\pi} \int_0^{2\pi} \frac{\cos(\theta)}{\left[|\alpha - R_0 \cos(\theta)|^2 + |\beta - R_0 \sin(\theta)|^2 + |\gamma - z_c|^2 \right]^{3/2}} d\theta \quad (2.2)$$

$$B_y = R_0 \frac{\mu_0 I (\gamma - z_c)}{4\pi} \int_0^{2\pi} \frac{\sin(\theta)}{\left[|\alpha - R_0 \cos(\theta)|^2 + |\beta - R_0 \sin(\theta)|^2 + |\gamma - z_c|^2 \right]^{3/2}} d\theta \quad (2.3)$$

$$B_z = R_0 \frac{\mu_0 I}{4\pi} \int_0^{2\pi} \frac{R_0 - \beta \sin(\theta) - \alpha \cos(\theta)}{\left[|\alpha - R_0 \cos(\theta)|^2 + |\beta - R_0 \sin(\theta)|^2 + |\gamma - z_c|^2 \right]^{3/2}} d\theta \quad (2.4)$$

A.2 Magnetic Field in a Helmholtz Coil

The point of this derivation is to determine the equation of a magnetic field for a Helmholtz coil at a point z , as well as the optimal separation between the two coils. Figure A.2 shows a generalized Helmholtz coil, with some unknown distance of separation d , and some point to calculate at, z .

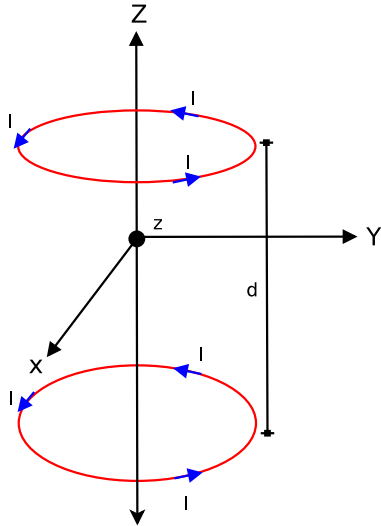


Figure A.2: Diagram of a Helmholtz coil, where the center is denoted by point z .

The easiest way to perform this derivation is to reduce this problem down to two individual coil problems, using the Biot-Savart law defined in Equation (2.1), then adding the two results together. Figure A.3 defines the vectors needed for calculating the magnetic field at some arbitrary distance z above the center of the coil. It is obvious that the maximum magnetic field produced by a single coil loop is going to be on-axis.

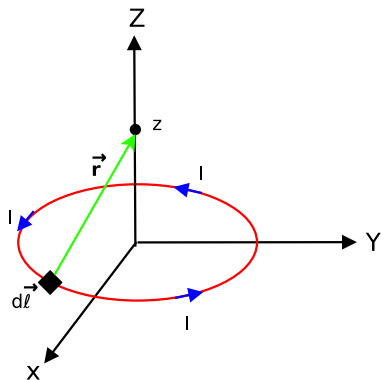


Figure A.3: Diagram of a single coil, where the center is denoted by point z .

From Figure A.3, the relevant vectors for the derivation are as follows:

$$\begin{aligned}\mathbf{r} &= -R \cos(\theta) \hat{i} - R \sin(\theta) \hat{j} + z \hat{k} \\ \ell &= R \cos(\theta) \hat{i} + R \sin(\theta) \hat{j} + z \hat{k} \\ d\ell &= -R \sin(\theta) d\theta \hat{i} - R \cos(\theta) d\theta \hat{j} + 0 \hat{k}\end{aligned}$$

Below, the cross-product of $d\ell \times \mathbf{r}$ was taken and expanded along the \hat{k} column.

$$\begin{aligned}d\ell \times \mathbf{r} &= \begin{vmatrix} \hat{i} & \hat{j} & \hat{k} \\ -R \sin \theta d\theta & R \cos(\theta) d\theta & 0 \\ -R \cos(\theta) & -R \sin(\theta) & 0 \end{vmatrix} \\ &= \hat{k} (R^2 \sin^2(\theta) d\theta + R^2 \cos^2(\theta) d\theta) \\ &= R^2 \hat{k} d\theta\end{aligned}$$

This result can then be used with the Biot-Savart law and integrated over the contour of the coil loop. This results in the B-field at point z for the bottom loop being

$$\begin{aligned}\mathbf{B} &= \frac{\mu_0 I}{4\pi} \int_0^{2\pi} \frac{R^2 d\theta}{(R^2 + z^2)^{3/2}} \hat{k} \\ \mathbf{B} &= \frac{\mu_0 I R^2}{(R^2 + z^2)^{3/2}} \hat{k}\end{aligned}\tag{A.2}$$

The Helmholtz Coil has two loops, with a coil below and the other above the point z . Therefore, since the magnetic field is a vector, simple addition of the two coils with Equation (A.2) provides the following result

$$\mathbf{B} = \frac{\mu_0 I R^2}{2} \left\{ \frac{1}{R^2 + (\frac{d}{2} + z)^2} + \frac{1}{R^2 + (\frac{d}{2} - z)^2} \right\} \hat{k}\tag{A.3}$$

Equation (A.3) gives the value of the magnetic field at the point z , though the distance between both of the coils is unknown. Therefore, the extrema of this equation needs to be found, in other words where $\partial \mathbf{B} / \partial z = 0$.

With the use of the chain rule on Equation (A.3), the following is the result

$$\frac{\partial \mathbf{B}}{\partial z} = \frac{\mu_0 I R^2}{2} \left\{ \frac{-3(\frac{d}{2} + z)}{\left[R^2 + (\frac{d}{2} + z)^2\right]^{5/2}} + \frac{3(\frac{d}{2} - z)}{\left[R^2 + (\frac{d}{2} - z)^2\right]^{5/2}} \right\} \hat{k}\tag{A.4}$$

In Equation (A.4), it's easy to see that $\partial \mathbf{B} / \partial z = 0$ if $z = 0$, meaning the extrema point is located in the middle of the two coils, at $z = \frac{d}{2}$. What is also desired is that this extrema point is also an inflection point, where

$\partial^2 \mathbf{B} / \partial z^2 = 0$ which would be the minimum rate of change of the slope, the inflection point of the magnetic field. Again, with the use of the chain rule on Equation (A.4), at the point $z = 0$, the result is the following

$$\begin{aligned}\frac{\partial^2 \mathbf{B}}{\partial z^2} &= \frac{3\mu_0 IR^2}{\left(R^2 + \frac{d^2}{2}\right)^{7/2}} \left(\frac{5d^2}{4} - \frac{d^2}{4} - R^2\right) \\ &= \frac{3\mu_0 IR^2}{\left(R^2 + \frac{d^2}{2}\right)^{7/2}} (d^2 - R^2)\end{aligned}\quad (\text{A.5})$$

Equation (A.5) fulfills the desired result of $\partial^2 \mathbf{B} / \partial z^2 = 0$ when $d = R$. Therefore, an inflection point will be at the center of the two coils if this relation holds true. Now that the values of z and d are known, the maximum value of the magnetic field from a Helmholtz coil can be calculated. This is done with Equation (A.3) by using the relations $z = 0$ and $d = R$.

$$\begin{aligned}\mathbf{B} &= \frac{\mu_0 IR^2}{2} \left\{ \frac{1}{R^2 + \left(\frac{R}{2}\right)^2} + \frac{1}{R^2 + \left(\frac{R}{2}\right)^2} \right\} \hat{k} \\ &= \frac{\mu_0 IR^2}{2} \left\{ \frac{2}{\left[\frac{5R^2}{4}\right]^{3/2}} \right\} \hat{k} \\ &= \frac{8\mu_0 I}{5^{3/2} R} \hat{k}\end{aligned}\quad (\text{A.6})$$

Equation (A.6) is for a Helmholtz coil comprised of only two loops. Normally, Helmholtz coils utilize more than a single coil, where each successive loop will carry a current I through it. Therefore, for a current with N loops in each section of the Helmholtz coil, the magnetic field would be

$$\mathbf{B} = \frac{8\mu_0 NI}{5^{3/2} R} \hat{k} \quad (\text{2.8})$$

APPENDIX B

SOURCE CODE

I didn't want to waste paper with printing this out, so all of the source code is available in a git-repository which is located at: <https://github.com/cmertin/Magnetic-Field-Simulation>

REFERENCES

- [1] Glenn F. Knoll. *Radiation Detection and Measurement*. Third. John Wiley & Sons, Inc., 2000, p. 232.
- [2] Glenn F. Knoll. *Radiation Detection and Measurement*. Third. John Wiley & Sons, Inc., 2000, p. 266.
- [3] Hamamatsu. *Photomultiplier Tubes: Basics and Applications*. 3a. 2007. URL: http://www.hamamatsu.com/resources/pdf/etd/PMT_handbook_v3aE.pdf.
- [4] Gerald L. Pollack and Daniel R. Stump. *Electromagnetism*. Pearson Education, Inc., 2002, p. 341.
- [5] Metglas. *Metglas Magnetic Alloy 2714A*.
http://metglas.com/products/magnetic_materials/2714a.asp.
- [6] amuneal Manufacturing Corp. *Magnetic Shielding Materials*.
<http://amuneal.com/magnetic-shielding/theory-design/magnetic-shielding-materials>.
- [7] Georgia State University. *Magnetic Properties of Ferromagnetic Materials*.
<http://hyperphysics.phy-astr.gsu.edu/hbase/tables/magprop.html#c2>.
- [8] Georgia State University. *Relative Permeability*.
<http://hyperphysics.phy-astr.gsu.edu/hbase/solids/ferro.html>.
- [9] Magnetic Shield Corp. *How Do You Measure Magnetic Fields In Gauss?*
<http://www.magnetic-shield.com/faqs-all-about-shielding.html>.
- [10] Orlokh Dorjkhaidav at Syracuse University. *Magnetic Shielding*.
http://physics.syr.edu/~orlokh/magnetic_shielding.PDF.
- [11] GREYC Engineering Research Laboratory. *Magnetic Shielding*.
<https://www.greyc.fr/sites/default/files/electronique/13%202012%20Shielding%20Allard%20SCHNABEL.pdf>.
- [12] Magnetic Shield Corp. *Does Cutting The Alloy Destroy Its Properties?*
http://www.magnetic-shield.com/pdf/does_cutting_the_alloy_destroy_its_properties.pdf.
- [13] Richard L. Burden and J. Douglas Faires. *Numerical Analysis*. Eighth. Thomson Brooks/Cole, 2005, p. 212.
- [14] Antonio de Bari. *Photomultiplier Tubes: principles & applications*.
http://www2.pv.infn.it/~debari/doc/Flyckt_Marmonier.pdf.
- [15] Magnetic Shield Corp. *B-H Curve*.
<http://www.magnetic-shield.com/science-research-and-education.html>.

- [16] Magnetic Shield Corp. *Online Calculator - Shield Size Vs. Source Field Strength*. URL: <http://www.magnetic-shield.com/science-research-and-education.html>.